



Instrument Science Report WFC3 2009-23

# WFC3 SMOV Program 11420: IR Channel Functional Tests

B. Hilbert & P. R. McCullough  
25 June 2009

---

## ABSTRACT

*Using data taken during Servicing Mission Observatory Verification (SMOV), we characterized the basic behavior of the IR Channel. Unless otherwise indicated, results in this report refer exclusively to those obtained during SMOV program 11420, with the IR detector temperature of -128 C. The correlated double sampling (CDS) read noise in RAPID sequences is 19.8 – 21.9 electrons, similar to the 20.0 – 22.0 electrons measured in TV3 (Hilbert 2008a), and equal to the Contract End Item (CEI) Specification of 21.2 electrons. The dark current measured from SPARS200 ramps is 0.030 – 0.048 e<sup>-</sup>/s/pixel, better than the CEI specification of <0.4 e<sup>-</sup>/s/pixel. From the internal flat fields through the F125W filter, we measured an inverse gain of 2.28 – 2.47 ± 0.04 e<sup>-</sup>/ADU, depending on quadrant. The ratio of the mean on-orbit instrumental irradiance (ADU/s/pixel) to ground test measurements is 1.06 – 1.07, indicating a brightening of the Tungsten lamp on orbit. We note there are differences in the signal rate of up to 3% between full frame flat field images and the smallest subarrays.*

---

## Introduction

SMOV tests of WFC3's cooled IR detector began in mid-June 2009. Program 11420, *IR Detector Functional Test*, was designed to measure the baseline performance and operability of the IR detector using only internal observations: darks and internal (WFC3 calsystem) flat fields. This report presents a summary of the current analysis of data from program 11420, and includes results of the read noise, dark current, system gain, and a preliminary characterization of the reference pixels. For convenience of analysis and data

comparison, the procedures and some figures and text used in ISR WFC3-2008-30 (Hilbert 2008) are reproduced in this report.

Program 11420 executed on June 24, 2009. All data were obtained with MEB2 using Science Mission Specifications (SMSs), i.e. no real time commanding. IR detector temperature was -127.9 C (145.1 K) and constant to within 0.2°C throughout program 11420. Most of the data was obtained in full-frame mode, although darks and flats were obtained also in each of the available subarrays in order to verify the operability of the subarray modes. All data were obtained at the nominal 2.5 e/ADU setting, although the measured (inverse) gain is lower than this value, and discussed below.

## Data

Visits 1-10 each acquired two full-frame dark current ramps using the BLANK in the filter wheel: a RAPID NSAMP = 15 followed immediately by a SPARS200 NSAMP = 15 from which we determined dark current, read noise, and reference pixel behavior. All dark current observations were made with the Channel Select Mechanism (CSM) in the IR position. Table 7 in Appendix 1 lists the files collected in each Visit, along with basic characteristics of each.

All data were processed using CALWF3 version 1.4.1 for basic data reduction. This included reference pixel subtraction, zeroth read subtraction, cosmic ray rejection, and non-linearity correction. The only change we made to the default behavior of CALWF3 when processing these data was to set the UNITCORR keyword to PERFORM. This sets the output values of the \*flt.fits files to units of ADU/sec, with values that are normalized to the appropriate exposure time of each pixel. If UNITCORR is set to its default of OMIT, the \*flt.fits files have values in ADU and each pixel contains the signal value of the final unrejected read (for example, if a pixel saturates in read #3, then that pixel in the \*flt.fits file will contain the signal value in read #2). This leads to an image that essentially has a variable exposure time from pixel-to-pixel and is not useful for analysis purposes. Tables 8 and 9 in Appendix 1 list the reference files used by CALWF3 for its processing steps. All measurements are reported on a quadrant-by-quadrant basis, following the previously defined convention for quadrant numbering illustrated in Figure 1.

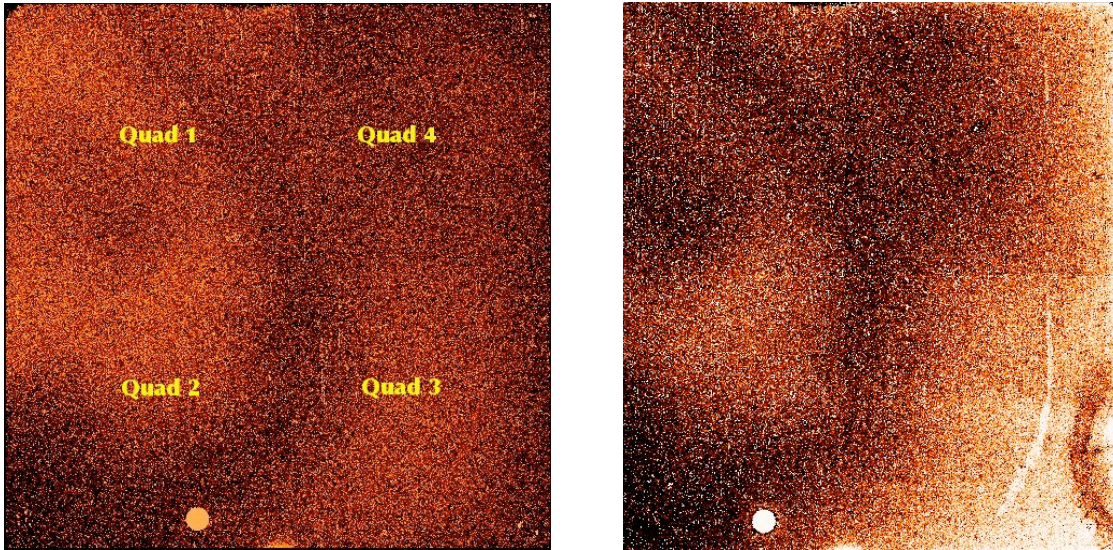


Figure 1: Dark current images from the final read of two 2800-second ramps (left TV3, right SMOV, Visit 9). Both images are the final read minus the zeroth read of a SPARS200 NSAMP=15 ramp and are displayed using a histogram equalization stretch, with pixel values ranging from -0.5 to 2.4 e-/sec/pixel. The circular feature at the bottom of quadrant 2 has been dubbed the "death star" and is a collection of poorly performing pixels. These pixels are ignored in all future calculations. Although the signal pattern across the detector is similar for these two images, the SMOV image shows generally higher (whiter) dark current values, associated with a light leak described below.

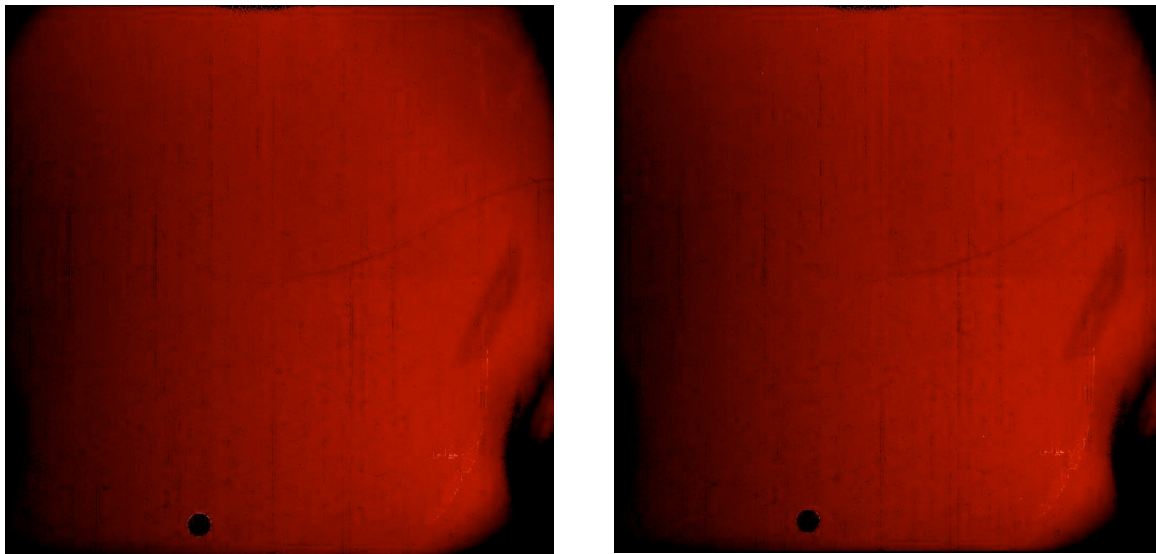


Figure 2: Internal full-frame flat field images with filter F125W and tungsten lamp (left TV3, right SMOV Visit 31, ramp iabg31e2q). Both images have been normalized to a mean value of 1.0. The stretch is linear with values ranging from 0 (black) to 1.42 (white).

## Analysis

### Light Leak

Analysis of observations from some Visits revealed contamination by an unidentified source of illumination that was not constant with time, even within a single ramp. See Figures 3 and 4 for an example. After comparing HST's orientation telemetry with times of exposure, we conclude that when HST was pointed at the day side of the Earth (hereafter referred to as the "bright Earth"), the IR detector was being illuminated by light leaking into the detector package. Figure 5 shows the relationship between the measured dark current rate and the angle between the limb of the Earth and the direction in which HST was pointing (called the V1 direction). When this angle is greater than zero (HST is pointed away from the Earth), the IR channel's measured dark rate is typically less than  $0.1 \text{ e}^-/\text{sec}/\text{pixel}$ . For images where this angle is less than zero (HST pointed at the Earth), the measured dark rate increases up to  $1 \text{ e}^-/\text{sec}/\text{pixel}$ .

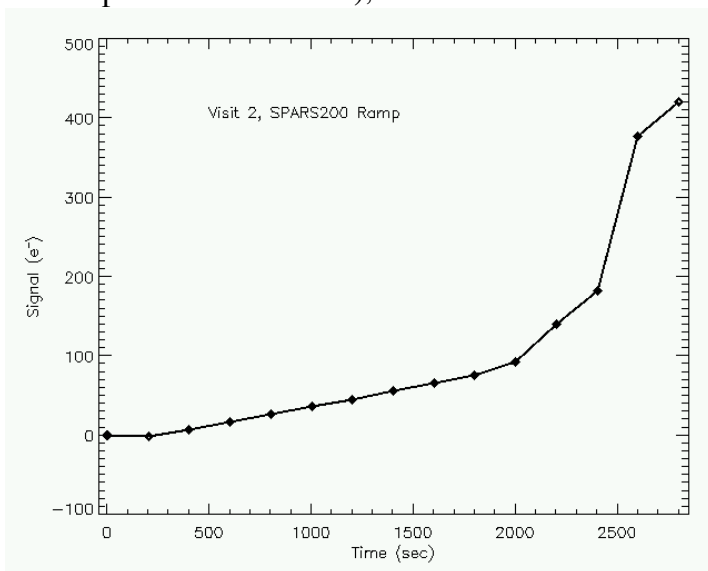


Figure 3: Mean signal in quadrant 1 for the Visit 2 SPARS200 ramp. The ramp appears nominal until between 1800 and 2000 seconds, where there is a slight increase in signal rate. After 2000 seconds there is a dramatic increase in signal rate, indicating the presence of the light leak.



Figure 4: Example image showing light leak in the Visit 2 SPARS200 ramp. This is an image of the last read minus the first read of the ramp. The scaling is identical to that in Figure 1. Histogram equalization stretch, ranging from -0.5 (black) to 2.4 (white)  $\text{e}^-/\text{s}/\text{p}$ . Note that the light leak affects the top half of the detector more than the bottom half. Vignetting is also apparent in a thin strip along the bottom edge of the detector.

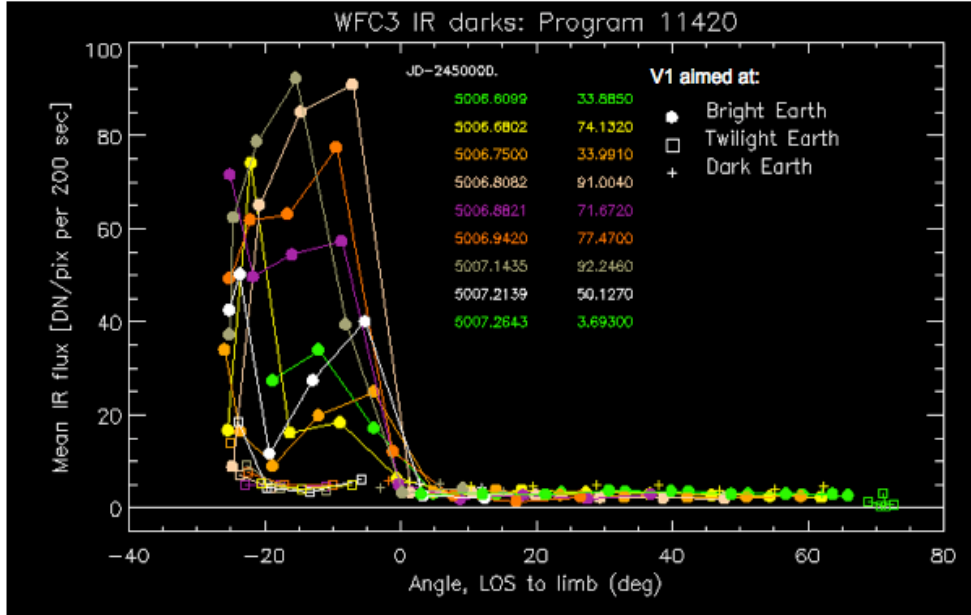


Figure 5: The mean flux (in ADU/pix per 200 sec interval) on the WFC3 IR array versus the angle between the line of sight (LOS) and the nearest limb of the Earth. (The LOS is HST's +V1 axis.) The peak flux corresponds to  $\sim 1$  e-/pixel and similar fluxes occur only when the +V1 axis is aimed at the brightly sunlit Earth (solid circles). Lower fluxes occur when V1 is aimed at Earth in twilight (open squares), and the lowest fluxes occur when V1 does not intercept the Earth (angle  $> 0$ ).

After careful analysis of the light leak affected data, we performed an experiment to limit the light leak. Beginning with Visit 5 of HST proposal 11447, the CSM was placed in the UVIS position when taking IR dark current measurements, thus directing any light incident on the CSM to the UVIS side of the instrument. Analysis of the data taken after this fix indicates that this is an effective method for mitigating the effects of the light leak in IR observations. The analysis results from proposal 11447 are detailed in Hilbert and McCullough (2009).

Rather than simply searching each ramp for global increases in signal rate, we developed a tool that collected information on HST's orientation and pointing direction relative to the position of the Earth. This information was plotted in such a way that we could easily tell if HST was pointed at the sunlit Earth during a given exposure. The details of what goes into the plot, as well as the quantities displayed in the plot, are given in a separate ISR (McCullough, 2009). An example plot is shown in Figure 6. This plot, corresponding to the SPARS200 dark ramp collected in Visit 2, shows that HST was above the bright Earth for almost the entire ramp, as indicated by the yellow open squares. However, HST was not pointing down at the bright Earth until roughly the final third of the ramp (filled yellow squares). Figure 4 shows the mean signal measured in this ramp. As expected, we see a slow accumulation of signal for the first two thirds of

the ramp, as expected. The final 5 reads however, show large increases in signal, as predicted in Figure 6.

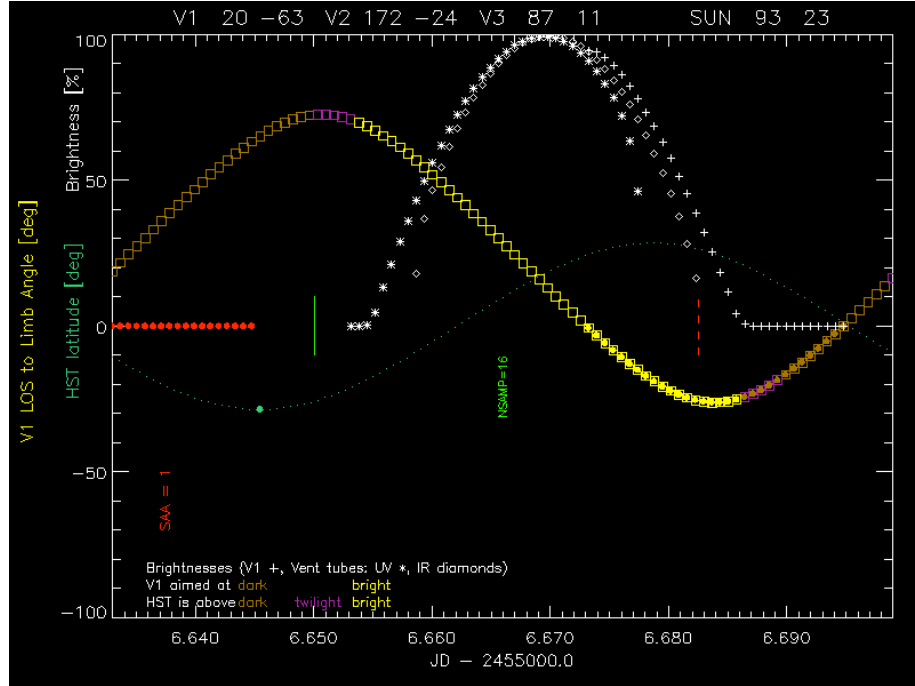


Figure 6: Plot showing the location and pointing direction of HST during the Visit 2 SPARS200 dark ramp. The filled yellow squares indicate that HST was pointed down at the bright Earth during the final third of the ramp.

The light leak fix was identified and tested only after all dark current data from this proposal were collected. Therefore a large fraction of the data discussed in this report is contaminated and are not useful for dark current analysis. Visits and individual files affected are identified in Table 7 using italics. Using the bright Earth prediction tool and plots such as that shown in Figure 6, we found that one full frame RAPID ramp (Visit 10) as well as 9 out of 10 full frame SPARS200 ramps are contaminated. The SPARS200 dark ramp from Visit 9 (shown in Figure 1, right panel) was predicted to be uncontaminated, although its non-nominal appearance suggests the presence of a light leak. Similarly, all but 5 subarray darks, collected in Visit 21, are contaminated. We ignore the contaminated exposures in the analysis of dark current presented below.

Unfortunately, our internal flat field ramps also suffered from a bright Earth-related light leak. Unlike the dark current ramps, the CSM is essentially in the UVIS position while taking IR internal flat fields, in order to place the diffuser paddle into the tungsten lamp's light path. Therefore we cannot eliminate this type of light leak by putting the CSM into a different position. We determined that all of the 64x64 and 128x128 subarray flat field ramps were contaminated by light leak. However, due to the short

exposure times of these images, and the fact that the light leak adds to a high signal from the tungsten lamp, we are able to use these subarray data to examine signal levels versus subarray size. However, these data were excluded from gain calculations due to the possibility of external noise from the light leaks.

### ***Internal Flat Fields***

We obtained flat field ramps through the F125W and F126N filters and illuminated by the tungsten lamp during Visit 31. Figure 2 shows an image of full frame F125W flat from these data next to one obtained during ground tests (TV3).

The SMOV and TV3 internal flat fields observed through filter F125W look the same, as do those for F126N (not illustrated). SMOV flats acquired in subarray mode look the same as the subarrays extracted from contemporaneous full-frame flats: proving that subarray readout patterns are nominal. We “blinked” the acquired subarray images with extracted subarrays and verified the location of the subarrays on the detector by identifying unique patterns of hot pixels (for the darks) and sensitivity variations (for the flats) in each quadrant and comparing their (X,Y) location in the subarrays with their locations in the full-frame images. The “blinking” process makes this comparison both trivial and thorough.

We compare the SMOV flat fields to those taken on the ground, in order to look for any differences in illumination pattern, signal level, etc. Figure 7 shows a ratio image of a full frame SMOV F125W internal flat to a similar TV3 flat. The image is shown with a histogram equalization stretch between 1.02 to 1.12, where blues represent the smaller values and reds and yellows show successively higher values. Figure 8 shows the histogram for each quadrant of the ratio image. The first result to note is that the mean value of the ratio in all quadrants is between 1.06 and 1.07, implying that the tungsten lamp has increased in brightness by 6-7% compared to ground testing. This is consistent with measurements made in the UVIS channel (Baggett, 2009). The shifts in the histograms with respect to one another indicate uneven illumination between the quadrants.

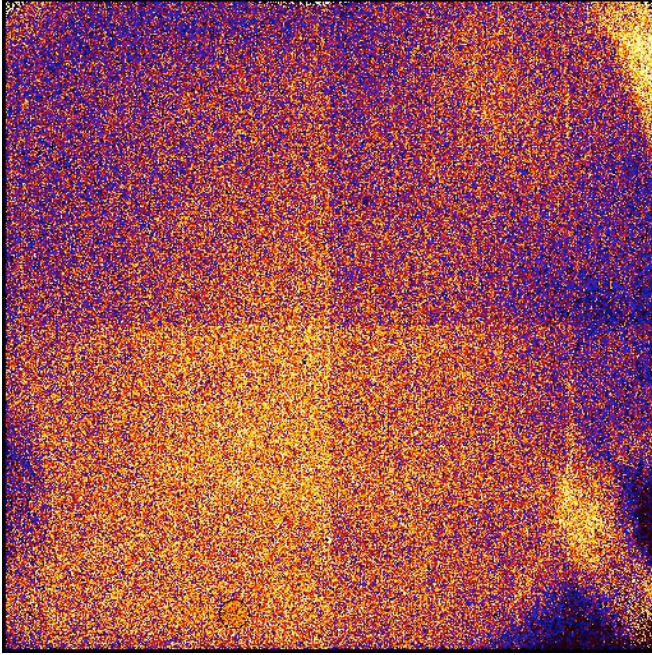


Figure 7: Ratio image of an F125W internal flat taken in SMOV to a similar image taken in TV3. This image is shown with a histogram equalization stretch with values between 1.02 and 1.12.

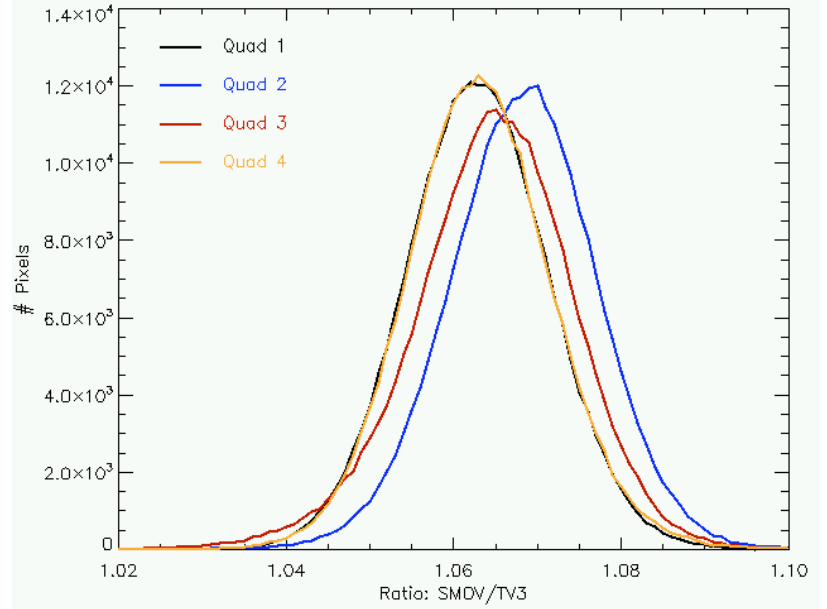


Figure 8: Histograms for the four quadrants of the image shown in Figure 7. Note the offset of the mean values from 1.0.

We next performed a similar comparison using the full frame and subarray flat fields taken as part of this proposal. Figure 9 shows histograms of the appropriate subarray extracted from the mean full frame flat versus mean subarray flats. We used flat images output from CALWF3 for these comparisons, so that we have measures of the signal rate in all cases. For each subarray size, we created a mean flat field from the 10 input ramps. This was done using IDL's *resistant\_mean.pro* on a pixel-by-pixel basis. In this case, we see that the subarrays have mean signal rates that are less than that of the same region in the full frame data. Table 1 lists the peak values and standard deviation of these distributions. The subarray images have exposure times much less than that of the full frame images (12.8 and 4.2 seconds for the 512 and 256 subarrays respectively), and therefore lower signal-to-noise levels. This explains the wider histograms for the smaller subarray, but not the overall shift of the histograms to lower levels.

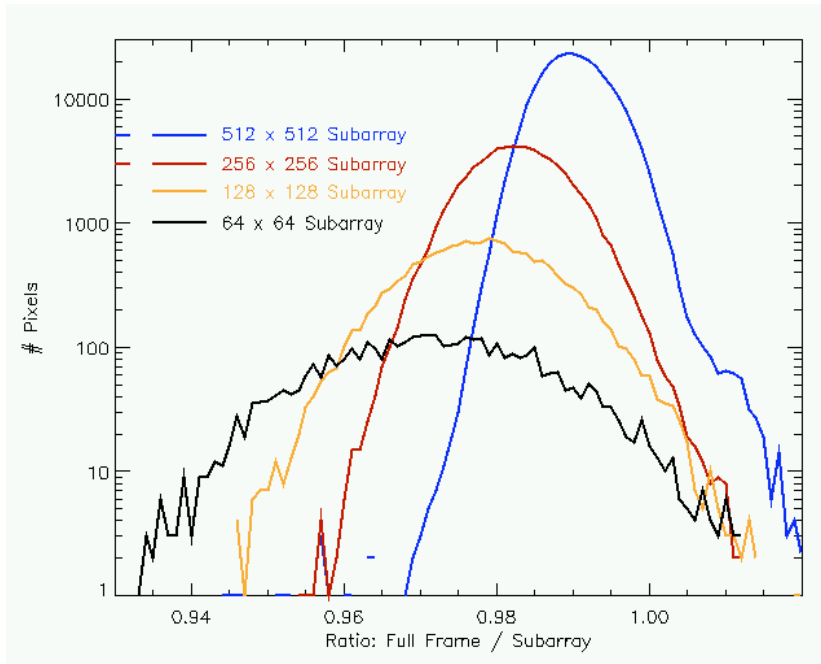


Figure 9: Histograms of the ratio between the full frame and subarray flat field images. Note that in all cases, the peak signal of the subarray is less than that of the full frame image. The full frame and each subarray image used to create these histograms are the mean of 10 individual images.

Subarray Size (pix)	Subarray Peak Signal VS Full Frame Peak Signal	Robust Standard Deviation of Distribution
512 x 512	99.0%	0.5%
256 x 256	98.2%	0.6%
128 x 128	97.9%	0.9%
64 x 64	97.0%	1.4%

Table 1: Peak values and robust standard deviations for ratios of mean subarray flat fields to the appropriate areas of the mean full frame flat.

### Gain

For the gain measurement we used all of the full frame, 512x512 and 256x256 subarray flat field data collected in Visit 31. The method used to calculate the gain is similar to that described in Hilbert (2008c). We created a photon transfer curve (PTC) (shown in Figure 10) using two ramps. The inverse of the best-fit line to these points

reveals the gain, in units of electrons per ADU. Once determined, the gain is applied to all data collected by the IR channel, converting measured counts into electrons.

Calculating the gain from ground testing data using this method proved challenging; and the same was true of the SMOV data. The PTC is a plot of the measured variance in the difference of two ramps versus the mean signal in the sum of those ramps. The challenge is to remove all inappropriate sources of variance from the data, including large scale fixed pattern noise, quadrant-to-quadrant variations in mean signal level, incomplete non-linearity correction, and pixels with a non-repeatable response to input signals. As sources of variance were removed from the data, the slope of the best-fit line decreased, leading to an increase in the measured gain.

We calculated gain values for each quadrant of the detector from groups of flat fields, shown in Table 2. The first was a set of 10 full-frame RAPID NSAMP=15 ramps taken using the F125W filter. The large bandpass of this filter allows signal to accumulate quickly. Similarly, we collected flat field ramps through the F125W filter using the 512x512 and 256x256 subarray modes. The exposure times of these modes were significantly less than for the full-frame data, so the total signal accumulated was much less. Finally, we collected flat fields using a lower irradiance, by using the F126N filter. The smaller bandpass limited the flux impinging on the detector. For these data we allowed signal to accumulate more slowly on the detector, with a suitably longer exposure time. For these ramps we used a SPARS50, 11 read sample sequence, with a total exposure time of 453 seconds per ramp. From these data, we examine the consistency of gain values measured at high versus low irradiance, as well as full-frame versus subarray modes.

For a given pair of input ramps, we first corrected for inter-pixel capacitance (IPC), which causes some of the signal measured by a pixel to be shared with its neighbors. (McCullough 2008) We applied a correction based on TV3 test results (Brown, 2008).

We then removed fixed pattern noise, which is due to differences in signal collection efficiencies across pixels. The result is a pattern of signal differences that is constant from one ramp to the next. (See page 30 of Janesik 2007 for a discussion of fixed pattern noise.) In order to remove this fixed pattern from our data, we divided the input ramps by a flat field taken through the same filter. For the F125W data, we created a median F125W flat field from the 10 ramps collected in this proposal. For the F126N data, we had only 3 ramps, and therefore divided the two input ramps by a flat field derived from the third.

We used a three step process to remove fixed pattern noise. As part of the default CALWF3 processing, all IR ramps have their zeroth read subtracted from all subsequent reads (Bond, 2007). As a way to avoid any reset-related effects adding noise to our measurement, we instead subtracted the first read of each ramp from the subsequent reads in that ramp.

Next, the signal levels in the two input ramps were normalized to the same mean level. This was done to account for any variations in lamp brightness or overall signal level between the two ramps. As discussed below, we did observe variations in the signal levels between the ramps in the full frame dataset, and these variations did have an effect on the final measured gain. By normalizing signal levels, we hoped to minimize any effects on variance.

Finally, we aggressively masked pixels with non-nominal behaviors. Any pixels identified by CALWF3 as hot, dead, unstable, saturated, or bad in the zeroth read were thrown out.

For each pair of input ramps, we then created 16 sum and difference images using all 16 reads up the ramp (ie read 16 of ramp 1 +/- read 16 of ramp 2). Examination of the difference images revealed residual fixed pattern noise along the left and right edges of the detector. To avoid this noise, we masked the “wagon wheel” area of the detector (lower right corner in the right panel of Figure 1), the rightmost 250 columns and leftmost 150 columns of the detector and the area around the “death star” (circular feature towards the bottom of the detector in Figure 1). These areas were ignored when making gain calculations.

Each set of sum and difference images, were divided up into 20x20 pixel boxes. For the summed images, each box was sigma-clipped at the  $3\sigma$  level, and IDL’s *resistant\_mean.pro* used to calculate a robust mean value for that box. Similarly for the differenced images, we sigma-clipped once at the  $3\sigma$  level within each 20x20 pixel box, and then used IDL’s *robust\_sigma.pro* to calculate the variance inside that box. We then plotted the mean and variance measurements for all boxes, as shown in Figure 10. The best-fit line to these data points for signals less than 24,000 ADU in the summed images (meaning less than 12,000 ADU in a single ramp) in order to eliminate non-linearity effects from the gain calculations (Hilbert, 2008c). And finally, for each read up the ramp, we sigma clipped the calculated variance values at the  $3\sigma$  level, in order to remove any boxes that happened to fall partially on portions of the detector that had been previously masked, or that had a large number of masked pixels.

At this point, we calculated a best-fit line to the remaining mean-variance points in each quadrant, and took the inverse of the best-fit slope as the gain for that quadrant. Figure 10 shows the mean variance values calculated for one ramp pair (diamonds). Red diamonds indicate values ignored in the line-fitting calculation, due to high signal or the sigma-clipping. Results from these gain calculations are given in Table 2.

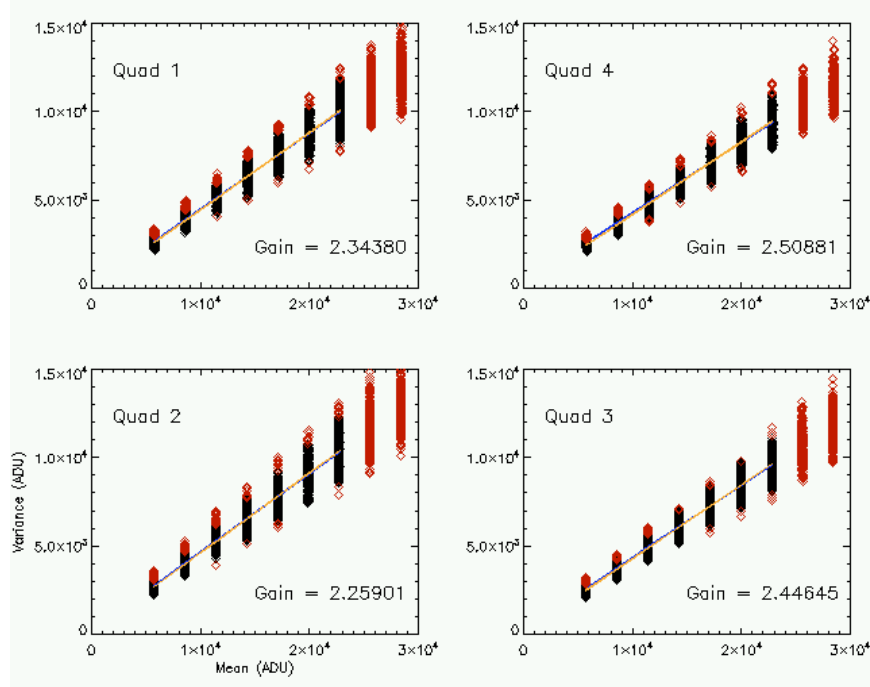


Figure 10: Photon transfer curves and best-fit lines for 4 quadrants of two F125W full-frame ramps. Black points were included in the line-fitting, while red points were excluded due to signal above the cutoff of 24,000 ADU, or having a variance value more than  $3\sigma$  from the mean at that signal level. The listed gain in each quadrant is the inverse of the best-fit slope.

### **Full Frame F125W Data**

Previous work on TV3 data showed a significant difference in the gain values depending on the relative time at which the two input ramps were taken. During ground testing, flat field ramps were dumped from the instrument in pairs, and Hilbert et al (2008c) found that gain values were significantly lower (implying higher variance values) when the two input ramps were in the same data dump. However, when the input ramps were the first ramps from two different data dumps, the measured gain values were higher (implying lower variance). The cause of this is unknown (Hilbert, 2008c).

We searched for similar effects in SMOV data, and found a dependence on ramp timing. SMOV data collection was the same as that in TV3 testing, where the F125W full frame flat field ramps were collected in pairs. Due to limited buffer space in the instrument, two flat fields were obtained consecutively and then the IR detector was placed in auto-flush mode while those two ramps were dumped from the instrument buffer. After the dump completed, two more ramps were collected, continuing the pattern.

Table 2 lists the gain values calculated from various datasets. Rows shaded red contain gain values from datasets where we believe we have removed all excess sources of variance. These gain values were used in the final calculation of a mean IR channel

gain. Rows in Table 3 shaded in blue contain gain values from datasets where we believe there are residual sources of variance in the data. These gain values were ignored in the calculation of a final mean gain value. Below, we step through the datasets listed in Table 2, explaining the analysis used in each.

The top row on Table 3 lists the mean gain value for pairs of full frame F125W input ramps that were taken consecutively. Interestingly, the calculated gain values are the same regardless of whether the input ramps are the two ramps within a single dump, or the second ramp of one dump followed by the first ramp of the next dump.

Compare these values to the gains reported in the second and third rows of the table. For these measurements, we used the every-other-ramp technique from TV3. The second row of the table shows the gain values for input ramps that were the first ramps in two consecutive data dumps. The third row of the table lists the gains when the input ramps were the second ramps of two consecutive data dumps. For example, if ramps A through D were taken in the order of: *A, B, data dump, C, D, data dump*, then the gain values reported in the second row of the table would be from pairing up ramps A and C, while the pair of ramps B and D would give gain values shown in row 3. Compare this to the first row of the table, where the gains would be from input pairs of *A,B*, or *B,C*, or *C,D*.

Pairing up first or second ramps from different data dumps (rows 2 and 3) both show statistically different, higher gain values than when pairing up consecutive ramps. The lower gain values from consecutive ramps imply some excess source of variance that was not removed. Figures 11 through 13 show plots that hint at the cause. Figure 11 shows the mean signal in each of the four quadrants in the 6<sup>th</sup> read of all 10 raw F125W flats. No line is drawn between data points when a data dump separated the two ramps. This is the mean signal before reference pixel subtraction and before zeroth read subtraction. In all quadrants, there is a very clear saw tooth pattern with an amplitude of 30-50 ADU between adjacent ramps. Ramps 4, 6, 8, and 10 all show a higher mean signal, and were all the second ramps in their respective data dumps. Ramps 3, 5, 7, and 9 show a lower mean signal, and were all the first ramps in their respective data dumps. Our theory is that the high signal put onto the detector in ramps 3, 5, 7 and 9 caused persistence, which added to the measured signal in ramps 4, 6, 8, and 10. The reverse is not true (ie high signal in ramp 4 did not cause persistence in ramp 5) because there was an 11-minute data dump between these ramps, during which any persistence effects had time to fade. At the same time, there does seem to be a long-term settling of the mean signal, as seen by the difference in signal level between ramps 3, 5, 7 and 9.

Filter/array size	Ramps Used for Input	Quad 1	Quad 2	Quad 3	Quad 4
F125W – full frame	Consecutive ramps*	2.28 +/- 0.02	2.23 +/- 0.02	2.40 +/- 0.02	2.42 +/- 0.02
	First ramps from data dumps (unaffected by persistence)	2.35 +/- 0.02	2.25 +/- 0.02	2.44 +/- 0.02	2.49 +/- 0.02
	Second ramps from data dumps (affected by persistence)	2.31 +/- 0.02	2.24 +/- 0.02	2.43 +/- 0.02	2.47 +/- 0.02
F125W – full frame, masked down to 512x512	Consecutive ramps*	2.29 +/- 0.02	2.29 +/- 0.02	2.42 +/- 0.02	2.42 +/- 0.02
	First ramps from data dumps (unaffected by persistence)	2.35 +/- 0.02	2.31 +/- 0.02	2.47 +/- 0.02	2.47 +/- 0.02
	Second ramps from data dumps (affected by persistence)	2.31 +/- 0.02	2.29 +/- 0.02	2.45 +/- 0.02	2.44 +/- 0.02
F126N – full frame		2.33 +/- 0.01	2.28 +/- 0.01	2.45 +/- 0.01	2.47 +/- 0.01
F126N – full frame, masked down to 512x512		2.32 +/- 0.01	2.34 +/- 0.01	2.47 +/- 0.01	2.46 +/- 0.01
F125W - 512 subarray	Consecutive ramps*	2.28 +/- 0.02	2.27 +/- 0.02	2.39 +/- 0.02	2.41 +/- 0.02
F125W - 256 subarray	Consecutive ramps*	2.29 +/- 0.05	2.29 +/- 0.06	2.31 +/- 0.04	2.28 +/- 0.04
<b>Mean SMOV Value (from red)</b>		<b>2.33 +/- 0.02</b>	<b>2.28 +/- 0.03</b>	<b>2.45 +/- 0.01</b>	<b>2.47 +/- 0.02</b>
<b>TV3</b>		<b>2.34 +/- 0.01</b>	<b>2.37 +/- 0.02</b>	<b>2.31 +/- 0.07</b>	<b>2.38 +/- 0.02</b>
<b>% difference</b>		<b>-0.4%</b>	<b>-3.8%</b>	<b>+6.1%</b>	<b>+3.8%</b>

Table 2: Gain values calculated from the various types of data in this proposal. Units are e-/ADU. Rows in red indicate values used in the calculation of the final mean SMOV gain values. Blue rows indicate gain values ignored when calculating the final mean gain. Uncertainties listed are the larger of the formal errors on the line-fitting process shown in Figure 10 or the robust standard deviation of the gain values of each data set. For some data sets (F126N, as well as the red rows for F125W full frame data), there were not enough ramp pairs to calculate a meaningful standard deviation. For these data, the listed uncertainties are the formal errors on the line-fitting, and represent a lower limit on the true uncertainty.

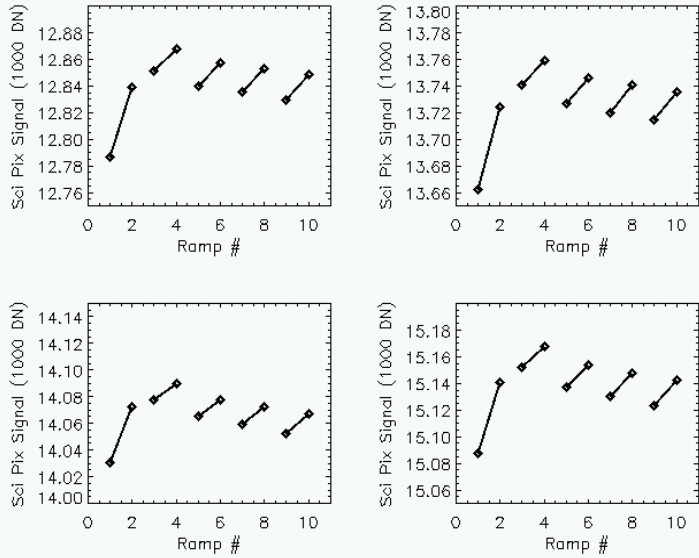


Figure 11: Mean signal in the sixth read science pixels for all ten full frame F125W flat field ramps. Breaks in the line indicate the positions of data dumps in the observing timeline.

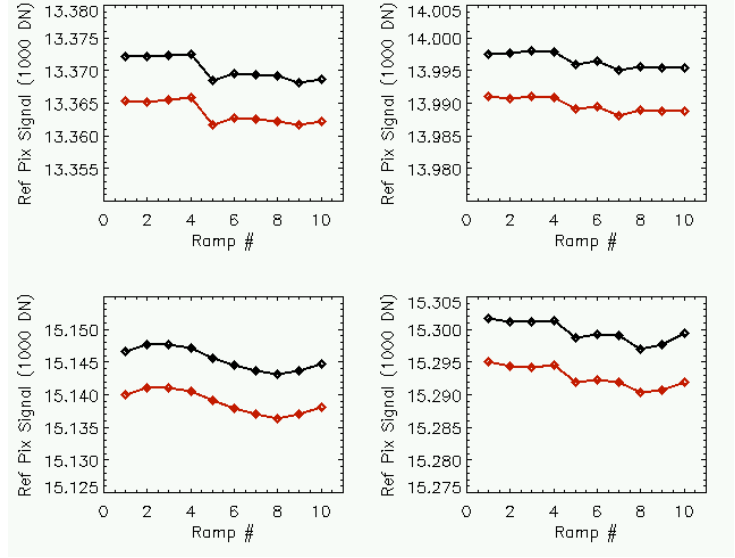


Figure 12: Mean signal in the sixth (black) and first (red) read reference pixels for all ten full frame F125W flat field ramps.

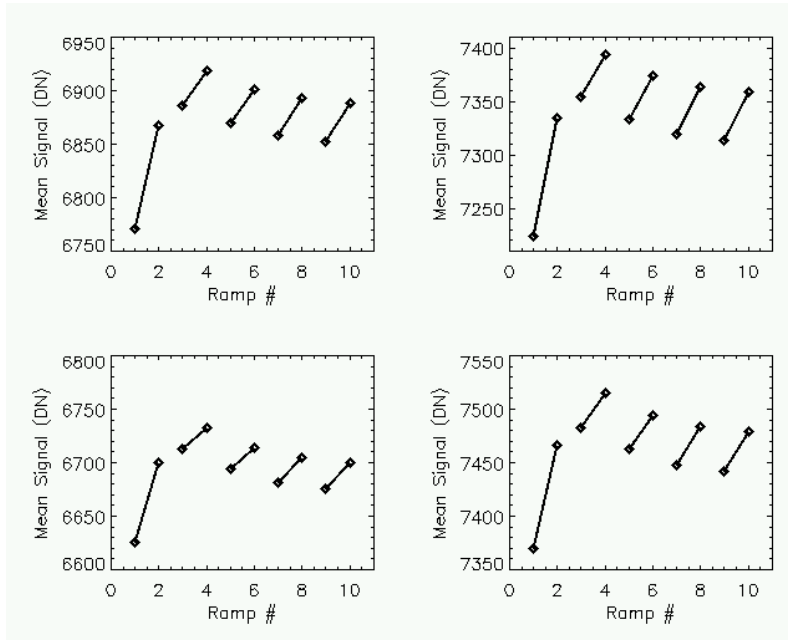


Figure 13: Reference pixel subtracted read six minus read one mean signal for all ten ramps. The reference pixels are unable to correct for what appears to be persistence.

Figure 12 shows the mean signal (calculated with *resistant\_mean.pro*) in the reference pixels of the four quadrants for all 10 ramps. The black curve shows the

reference pixel signals in the first read of each ramp, while the red curve is for the 6<sup>th</sup> read of each ramp. No saw tooth pattern is visible here, and the magnitude of the variations from ramp to ramp are much less than in Figure 11. As this suggests, in Figure 13 we see that subtracting the reference pixel values from the science pixels does not remove the saw tooth pattern seen in Figure 11. In Figure 13 we plot the mean reference pixel subtracted signal in read 1 from the reference pixel subtracted signal in read 6, mimicking the steps performed in CALWF3. The saw tooth pattern remains, with an amplitude of roughly 50 ADU.

These plots suggest that using consecutive ramps from the full-frame F125W dataset to calculate gain will result in an excess variance, that will artificially drive the measured gain down. Therefore for the final SMOV gain values quoted in Table 2, we do not consider gains calculated from the top row. Nor do we consider gains calculated using ramp 1, as its mean signals also deviate from those of the rest of the dataset.

Instead, we focus on rows 2 and 3 of Table 2. Row 2 shows the mean gain values calculated using ramps unaffected by persistence, according to our theory. This corresponds to ramps 3, 5, 7, and 9 in Figures 11 through 13. Row 3 in Table 2 shows the gain values calculated using the ramps that are affected by persistence. Comparing these two rows in the table we see very similar gain values, with differences of at most 2% (in quadrant 1). Unfortunately, in both the persistence affected and unaffected cases, 4 ramps meant we were only able to create 2 pairs of ramps. This implies that our uncertainties in both measurements are not well known. Uncertainties from the line-fitting in Figure 10 imply an uncertainty any single gain measurement of  $0.01 \text{ e}^-/\text{ADU}$  for all full-frame data. From the variation in gain values observed when ignoring persistence and pairing consecutive ramps, we expect the uncertainty to be  $0.02 - 0.03 \text{ e}^-/\text{ADU}$ .

### *Subarray Data*

We then checked the other flat field data in this proposal for similar effects. We looked first at the ten ramps through the F125W filter using the 512x512 subarray. All ten ramps were obtained with no break in the observing. Therefore, we do not expect to see a pattern like that in Figure 11. Figure 14 shows the mean raw signal value in the 6<sup>th</sup> read of the 512x512 subarrays. Unlike the full frame data, here we see a constant increase in the mean read 6 signal value. Figure 15 shows the reference pixel subtracted mean signals for read 6 minus read 1. Here we see that the increase in signal with time has been corrected, leaving behind no obvious pattern in all four quadrants, as expected. From this, we conclude that it is safe to calculate gain values using consecutive 512x512 subarray ramps.

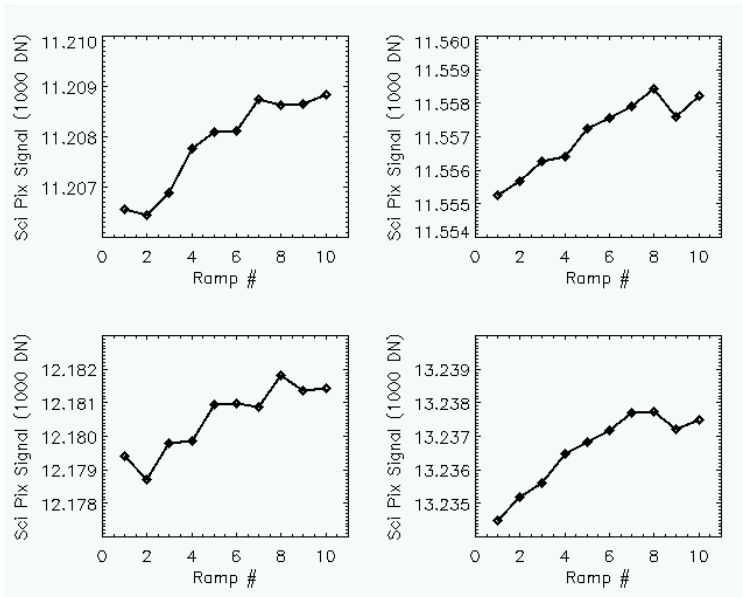


Figure 14: Mean signal in the sixth read of the raw science pixels for the ten F125W 512x512 subarray ramps. There were no pauses in data collection during this data set.

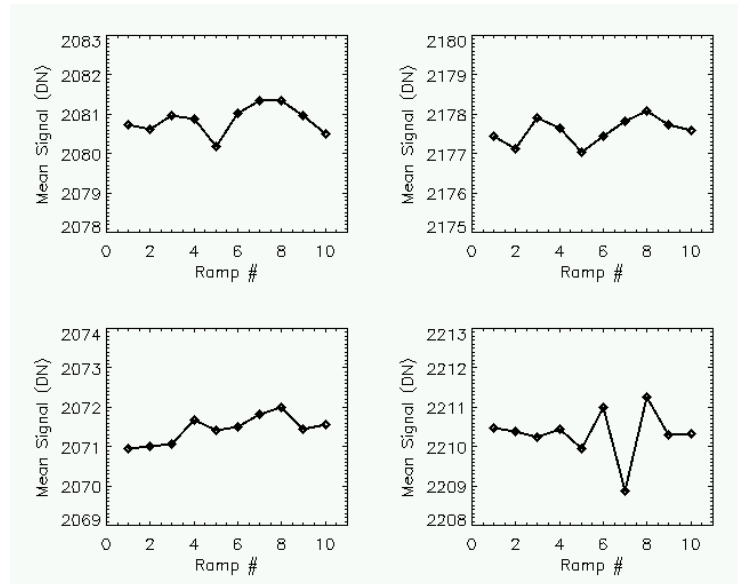


Figure 15: Reference pixel subtracted, read 6 minus read 1 mean signal for the same ramps. The reference pixels have corrected for the non-zero slopes seen in Figure 14, so that all ten ramps are at a consistent signal level.

For the 256x256 subarray data, we find a similar behavior. Timing values in the headers indicate that there were two breaks in the data collection for the 256x256 subarrays. The first two ramps were collected, followed by a 2-minute break. Six more ramps were then collected, followed by a 3-minute break and then the final 2 ramps. Figure 16 shows the mean raw signal in read 6 of the 256x256 subarray ramps. Again here, breaks in the line indicate the positions of the breaks in observing. Here we see what appears to be a similar pattern to the full frame data, where the first ramp after a break in observing has the lowest mean signal. However, unlike the full frame case, the reference pixel subtraction is able to correct for this effect here. Figure 17 shows the mean signal in the reference pixel subtracted read 6 minus read 1 image. Here we see that the variations in mean signal far from the observing breaks are comparable to those near the observing breaks, suggesting that the reference pixel subtraction effectively removed any pattern. There are hints of a saw tooth pattern in this figure, although it is inconsistent from quadrant to quadrant. Note that the range of mean signal variations in this case is very small ( $<1$  ADU). The exposure time of these 256x256 subarray ramps is roughly a factor of 10 less than the full frame ramps. However, the variation in signal seen here is approximately a factor of 50 less than that in the full frame data. Given these results, we assume it is safe to calculate gain values from consecutive 256x256 subarray ramps.

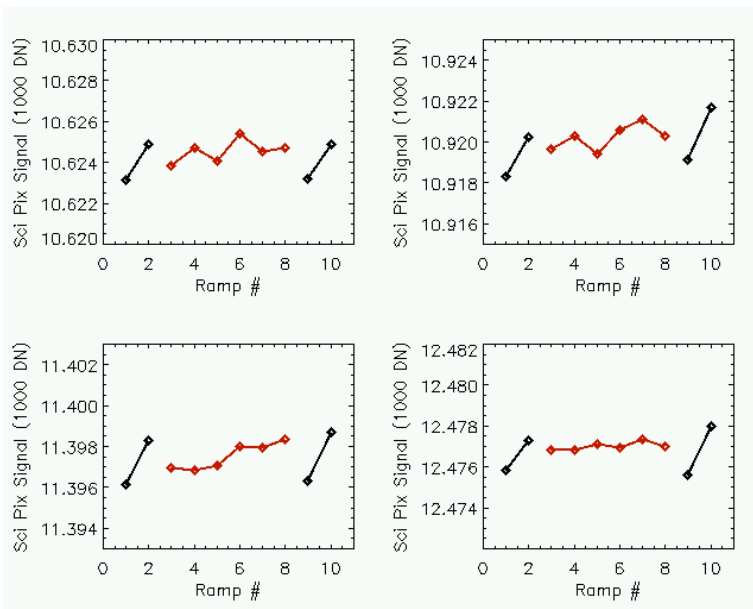


Figure 16: Mean signal in the raw sixth read science pixels for all ten F125W 256x256 subarray ramps. There were two short (2-3 minute) breaks in data collection, between ramps two and three, as well as eight and nine. There are indications of persistence, similar to that seen in the full frame data in Figure 11.

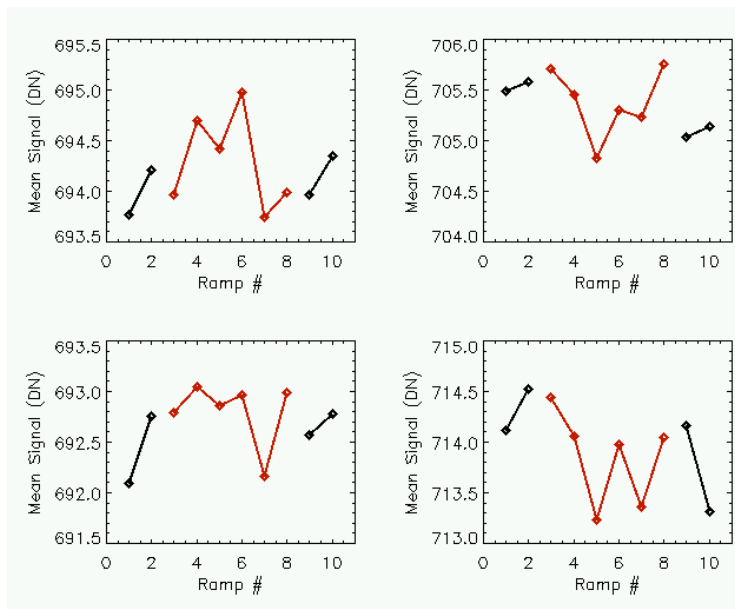


Figure 17: Mean signal in the reference pixel subtracted read 6 minus read 1 frames. Remaining ramp-to-ramp variations in the signal are less than 2 ADU.

### Low Irradiance Flat Field Data

The final dataset to check were the low-irradiance flat fields collected through the F126N filter. In this case, we obtained only 3 ramps. The exposure time of these ramps was long enough that WFC3 was able to simultaneously dump a ramp while collecting the next. Therefore there were no breaks between the three observations. Figure 18 shows the mean raw read 6 signal for the 3 ramps. Figure 19 shows the reference pixel subtracted read 6 minus read 1 signal. Again, we see a similar pattern to that in the F125W full frame data, where the first ramp of the group has the lowest mean signal even after reference pixel subtraction. In this case, with no break between the next two ramps, we see a nearly identical mean signal in these two ramps. From this, we concluded (and tested to verify) that the only reliable gain values that could be calculated with this 3 ramp dataset was to use the second and third ramps to create the sum and difference images, and used the first ramp only as a flat field to remove fixed pattern noise from both.

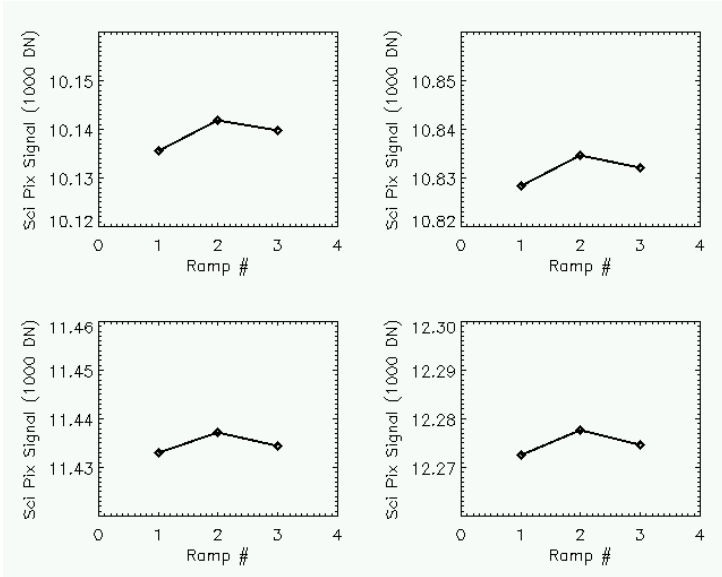


Figure 18: Mean signal in the raw read 6 science pixels for the three F126N flat fields.

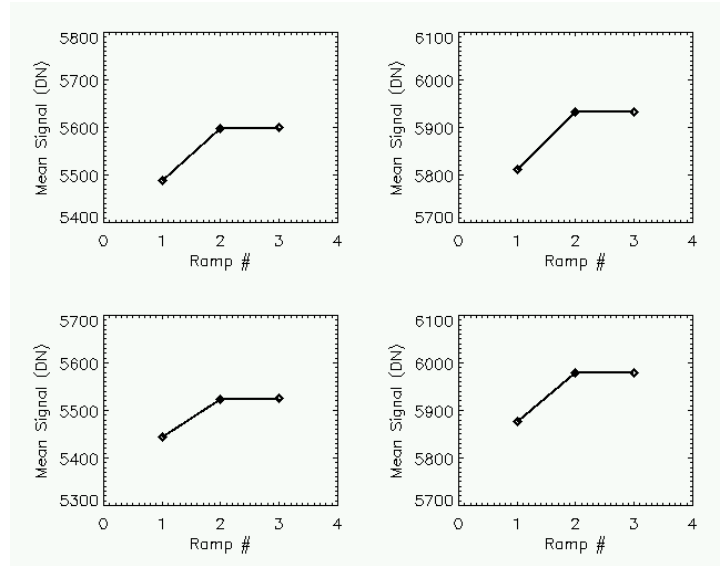


Figure 19: Mean signal in the reference pixel subtracted read 6 minus read 1 science pixels. Similar to the F125W full frame data, the first ramp shows a depressed mean signal compared to subsequent ramps. Unlike the F125W full frame data, there is no break in data collection here, and the second and third ramps show a consistent signal level.

As a consistency check, we also took the full frame F125W and F126N flat fields and masked the outer pixels until we cut them down to 512x512 pixels. We then re-measure the gain of these pseudo-512x512 subarrays, in order to compare the answer with the full frame gains as well as the true 512x512 subarray data. We also consider these gain values to be reliable given that we found the full frame pairs to provide reliable gain values. In most cases, the pseudo-512x512 subarrays gave gain values statistically identical to those obtained from the full frame data. Quadrant 2 showed the worst match, with the pseudo 512x512 subarray gains lower than those from the full frames by up to 2.5%.

Gain values calculated using the true 512x512 and 256x256 subarrays were consistently lower than those from the full frame F1215W data. This was especially true in quadrants 3 and 4, where the differences were as much as 8%. However, with their shorter exposure times of only 30% and 10% of the full frame exposure time, we expect the signal to noise of the full frames to be approximately 2 and 3 times that of the 512x512 and 256x256 subarrays, respectively. Also, the line fitting shown in Figure 10 was performed over a smaller signal range for the subarray data compared to the full frames, leading to the larger uncertainties shown in Table 2. Additionally, Table 1 shows that the measured signal rate in the subarray flats was less than that in the full frame ramps by up to 3%. As can be seen in the photon transfer curve in Figure 10, a decrease

in the mean signal values has the same effect as an increase in the variance values, in that the slope of the best-fit line will increase, causing a decrease in the measured gain. Therefore, these lower observed signal rates are consistent with lower measured gain values.

For this reason, we have decided to exclude the subarray data for the purposes of calculating the overall mean gain values from this proposal. Therefore, using both the full frame F125W and F126N data, combined with the gains produced from masking that full frame data down to 512x512 subarrays, we calculate the mean IR channel gain values shown towards the bottom of Table 2. For comparison, gain values derived from TV3 ground testing data are also shown, along with the difference between TV3 and SMOV values. We believe the modifications made to the gain calculation method during this data analysis have resulted in a more robust measure of the IR channel's gain values compared to the values calculated from TV3 data.

### ***Read Noise***

As was done with TV3 data, we calculated two measures of noise for the IR channel from the data taken in this proposal. (Hilbert, 2008a) The first is CDS noise, and the second is “effective noise”. CDS noise is the measure of the standard deviation in a difference image created from two consecutive reads within a ramp, while effective noise provides a measure of the noise after all reads of a ramp have been combined to form a final image.

CDS and effective noise values were calculated using the same method as was used on TV3 data. Results from that test are detailed in (Hilbert, 2008a). CDS readnoise values were calculated using the RAPID-15 dark current ramps taken in Visits 1 through 9. The RAPID ramp from Visit 10 was excluded due to the presence of the light leak. For each 15 read ramp, we created 14 difference images using consecutive reads. We then created a histogram of the values in each difference image, and performed a Gaussian fit in order to calculate the width (Gaussian sigma, using Markwardt's *mpfitpeak.pro*<sup>1</sup>) of the histogram. This provided a measure of the total noise in the difference image. However, this measured noise included contributions from both the read noise and shot noise from dark current signal. In order to remove the dark current contribution to the noise, we first determined the dark current in each pixel by fitting a line to that pixel's signal through the 15 reads of the ramp. The slope of this line gave us

---

<sup>1</sup> Available at <http://www.physics.wisc.edu/~craigm/idl/fitting.html>

Copyright (C) 1997-2001, 2003, 2005, 2007, 2008, 2009, Craig Markwardt

This software is provided as is without any warranty whatsoever. Permission to use, copy, modify, and distribute modified or unmodified copies is granted, provided this copyright and disclaimer are included unchanged.

the dark current rate for that pixel. We then multiplied this rate by the exposure time between two consecutive reads in the ramp. For the case of the RAPID ramps, this was 2.9 seconds. This gave the total dark current signal that accumulated between the two reads. The square root of this signal is the dark current shot noise contribution. By subtracting the square of the dark current noise (ie the dark current signal) from the square of the total measured noise from the histogram fitting, and taking the square root of the result, we obtained a measure of the true CDS readnoise. Equation 1 shows this calculation. Here,  $RON$  is the CDS readnoise that we wish to calculate.  $noise$  is the total noise measured with the histogram fitting.  $r$  is the dark current rate, and  $t$  is the exposure time between consecutive reads.

$$RON = \sqrt{noise^2 - (r \times t)^2} \quad 1)$$

For short ramps, like RAPIDs, the subtraction of the dark current shot noise has no significant effect on the measured readnoise. However for longer ramps, there is a noticeable effect. We repeated this calculation on all 14 difference images for a given ramp, and then took the median of these values as the CDS readnoise for that ramp. Figure 20 shows the CDS readnoise values calculated for all RAPID ramps in this proposal, and Table 3 reports the mean readnoise values for the dataset.

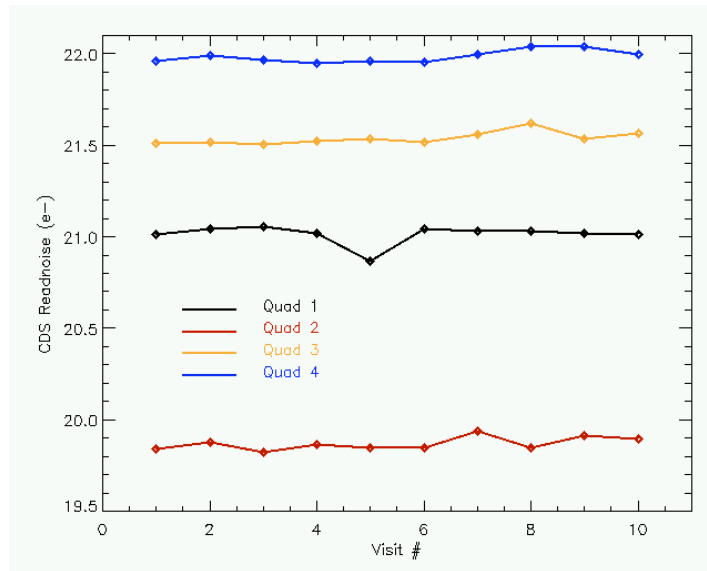


Figure 20: Calculated CDS readnoise values for the 10 RAPID dark current ramps collected in this proposal. The ramp in Visit 10 was contaminated by light leak, but its readnoise appears unaffected due to the short exposure time.

We converted the values from ADU to electrons with the mean SMOV gain values in Table 2. The CDS readnoise values for each quadrant are reported in Table 3. For comparison, we also show the CDS readnoise values measured in TV3 testing, where we have converted the values given in Hilbert (2008a) to the SMOV gain values. For all 4 quadrants, the CDS readnoise values from SMOV testing are comparable to those from ground testing.

By the same process we evaluated CDS read noise for the Visit 9 SPARS200-15 ramp and report those values in Table 3 also. Again, the SMOV CDS readnoise values are similar to those calculated in TV3. Due to the long exposure time between reads (200 seconds) other sources of noise push the measured CDS readnoise of the SPARS200 ramps above that of the RAPID ramps.

CDS Readnoise ( $e^-$ )				
	Quadrant 1	Quadrant 2	Quadrant 3	Quadrant 4
RAPID SMOV	21.03 +/- 0.02	19.87 +/- 0.04	21.53 +/- 0.03	21.99 +/- 0.04
RAPID TV3 (converted to SMOV gain)	20.8	20.0	21.8	22.0
SPARS200 SMOV	22.39 +/- 0.29	21.33 +/- 0.17	23.08 +/- 0.16	23.41 +/- 0.06
SPARS200 TV3	22.2	21.4	22.8	23.2

*Table 3: CDS readnoise values measured in SMOV versus those measured in TV3 ground testing. For ease of comparison we took the TV3 values presented in Hilbert (2008a) and converted them to the SMOV gain values measured in this proposal. The uncertainty on the CDS measure for a single SMOV ramp was  $0.06 e^-$ . Ten RAPID ramps were averaged together to give the values in this table. The uncertainties given are the robust standard deviation of the set of readnoise measurements. For the SPARS200 ramp, the stated uncertainties are the robust standard deviations of the readnoise values measured for all CDS pairs up the ramp. Uncertainties in TV3 readnoise values are assumed to be similar to those derived from SMOV data.*

The second type of noise calculated from these data was effective noise. This is a measure of how well the noise averages down in a given ramp compared to the number of reads used to create a final image. Similar calculations were performed on ground testing data, the results of which are detailed in Hilbert (2008a). To calculate the effective noise for a ramp, we begin by fitting a line to the signal in each pixel up the ramp. This is the same method that CALWF3 uses to create a final image (stored in the flt file) from a data ramp (stored in the ima file). By multiplying the formal uncertainty in the best-fit slope by the exposure time of the ramp, we arrive at a measure of the noise associated with that pixel in the final image. We then create a histogram of these effective noise values and fit a Gaussian to the distribution in order to determine the position of the peak. The

histogram peak positions are the values reported in Table 4 and shown by the red curves in Figures 21 and 22. By varying how many reads of the ramp we use in the line-fitting, we are able to determine the effective noise in ramps of any length.

Figure 21 shows the measured effective noise for the Visit 9 SPARS200 ramp. The blue line shows the measured CDS readnoise for quadrant 2 of that ramp. The red line shows the measured effective noise versus the number of reads used to create the final image. We see that when using all 16 reads (corresponding to NSAMP=15 plus the zeroth read) the final image has an effective noise of  $11.7 e^-$ . Figure 22 shows the results for calculations performed on the Visit 9 RAPID ramp. The effective noise of the RAPID ramp appears to decrease slightly more quickly than that of the SPARS200 ramp, and finishes at a value of  $11.4 e^-$  when using all 16 reads. Table 4 lists the measured effective readnoise values for all quadrants measured using data from this proposal, as well as the values calculated in TV3 testing, for comparison.

Quads 2 through 4 show comparable noise values between TV3 and SMOV for the RAPID ramps, while quad 1 shows elevated noise values in SMOV. For the SPARS200 ramp however, the effective noise values are consistently lower in SMOV than they were in TV3. This difference between long and short exposure ramps implies a decrease in an unidentified time-dependent noise source.

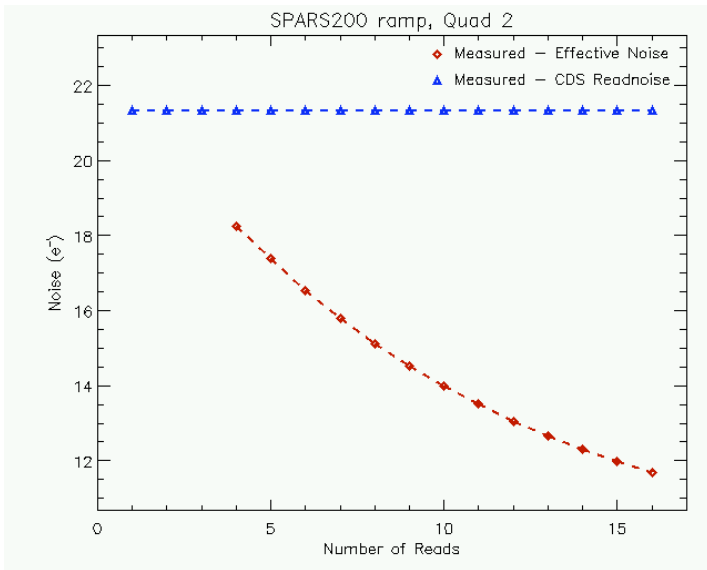


Figure 21: Effective noise for a SPARS200 dark ramp. Using all reads to create the final image, we find an effective noise of  $11.7 e^-$ .

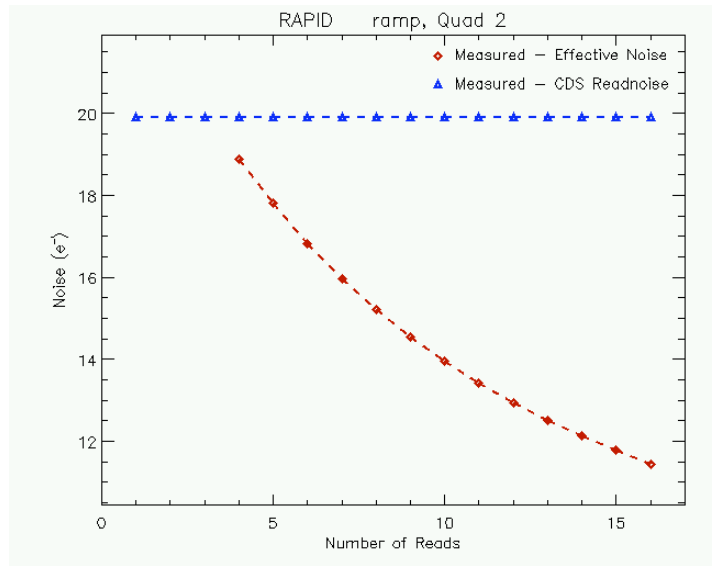


Figure 22: Effective noise for a RAPID dark ramp. Combining all reads in the ramp, the effective noise is  $11.4 e^-$ .

	<b>Quad 1</b>	<b>Quad 2</b>	<b>Quad 3</b>	<b>Quad 4</b>
<b>SMOV SPARS200</b>	19.5 / 15.9 / 12.3	18.6 / 15.1 / 11.7	20.1 / 16.4 / 12.6	20.4 / 16.6 / 12.8
<b>TV3 SPARS200</b>	20.5 / 17.5 / 14.4	20.1 / 17.1 / 14.1	21.6 / 18.4 / 15.1	21.2 / 18.1 / 15.0
<b>SMOV RAPID</b>	21.0 / 16.1 / 12.1	19.9 / 15.2 / 11.4	21.5 / 16.4 / 12.4	22.0 / 16.8 / 12.6
<b>TV3 RAPID</b>	19.3 / 15.2 / 11.5	19.5 / 14.9 / 11.2	20.9 / 16.0 / 12.0	21.9 / 16.7 / 12.6

*Table 4: Effective noise for SMOV and TV3 data. The three numbers in each cell represent the effective noise when using 3, 8, and 15 reads to create a final image. Units are electrons. Formal uncertainties are less than  $0.1 e^-$ . TV3 values have been collected from Hilbert (2008) and converted from the gain used in that analysis ( $2.26 e^-/ADU$ ) to the values listed in Table 2. SMOV RAPID values are the mean of the values calculated for Visits 1 through 9.*

### ***Dark Current***

Only one of our SPARS200 dark current ramps (Visit 9) was unaffected by the bright Earth light leak. As discussed below, this single ramp showed anomalously low dark current in comparison to TV3 values, and had a non-nominal appearance, as seen in Figure 1 (right panel). Further IR channel dark current analysis, based on data from SMOV proposal number 11447, is presented in Hilbert and McCullough (2009). Figure 23 shows a plot of the mean signal values in quadrant 1 for our Visit 9 SPARS200 ramp, as well as the mean SPARS200 ramp derived from TV3 data (where the TV3 values have been converted to the gain measured in this study). The SMOV ramp shows a much lower rate of signal accumulation compared to the TV3 ramp. The reason for this is not known. Analysis of HST's orientation during this ramp indicated that HST was located above the bright Earth, but pointed away from the Earth. As the exposure progressed, HST's line of sight approached the limb of the bright Earth. The exposure ended approximately one to two minutes before HST's line of sight crossed the Earth's limb. From this, we expect that any light leak effects should be minimal. But we see nothing to suggest a lower than expected dark current rate.

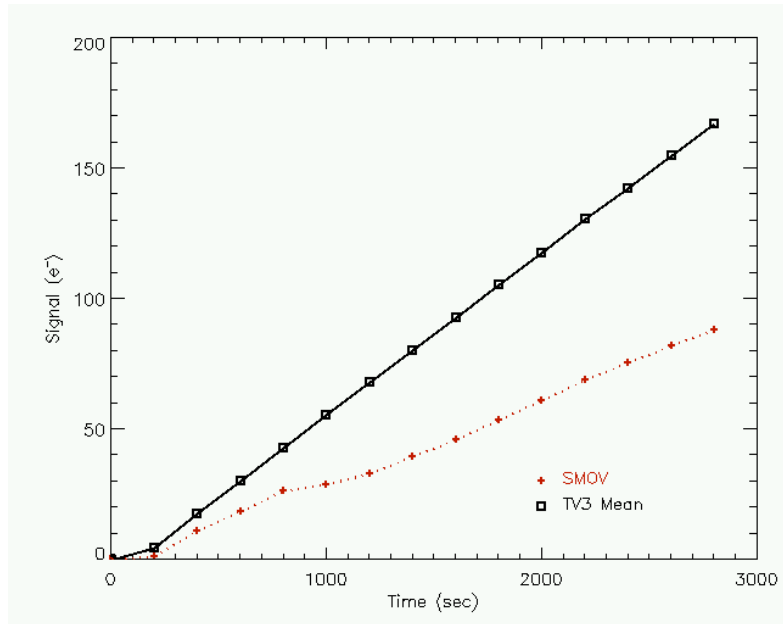


Figure 23: Robust mean signals up the ramp for quadrant 1 of the Visit 9 SPARS200 ramp observed during SMOV (+ signs) compared to the CDBS SPARS200 dark (t611932fi\_drk.fits) derived from TV3 data (squares).

Dark current rates were calculated by CALWF3 through line-fitting to 14 reads of each pixel. CALWF3 ignores the first read of the ramp in order to avoid any reset anomaly effects, such as those described by Hilbert (2008b). Examination of the measured signal in the first two reads of the SMOV data in Figure 23 suggest that the elevated signal in the initial read seen during TV3 testing remains in data taken on orbit. We note that the effects of this anomaly will be removed from WFC3-IR data by CALWF3 in the data reduction process, because dark current ramps are subtracted on a read-by-read basis from data ramps.

We next created a histogram of the dark current rates in each quadrant of the Visit 9 SPARS200 ramp, as well as the mean SPARS200 ramp from TV3 testing. The peak position of a Gaussian fit to the histogram was recorded as that quadrant's "mean" dark current rate, which will be slightly smaller than the true median, due to the long tail of hot pixels. This process and definition are identical to those adopted by Hilbert (2008b) which includes an illustration of a typical histogram and Gaussian fit for a SPARS200 ramp such as those analyzed here also. The resulting dark rates along with the robust standard deviation of the dark rates in each quadrant are given in Table 5. The histograms are shown in Figure 24. The Visit 9 dark ramp exhibits lower than expected dark current in all four quadrants.

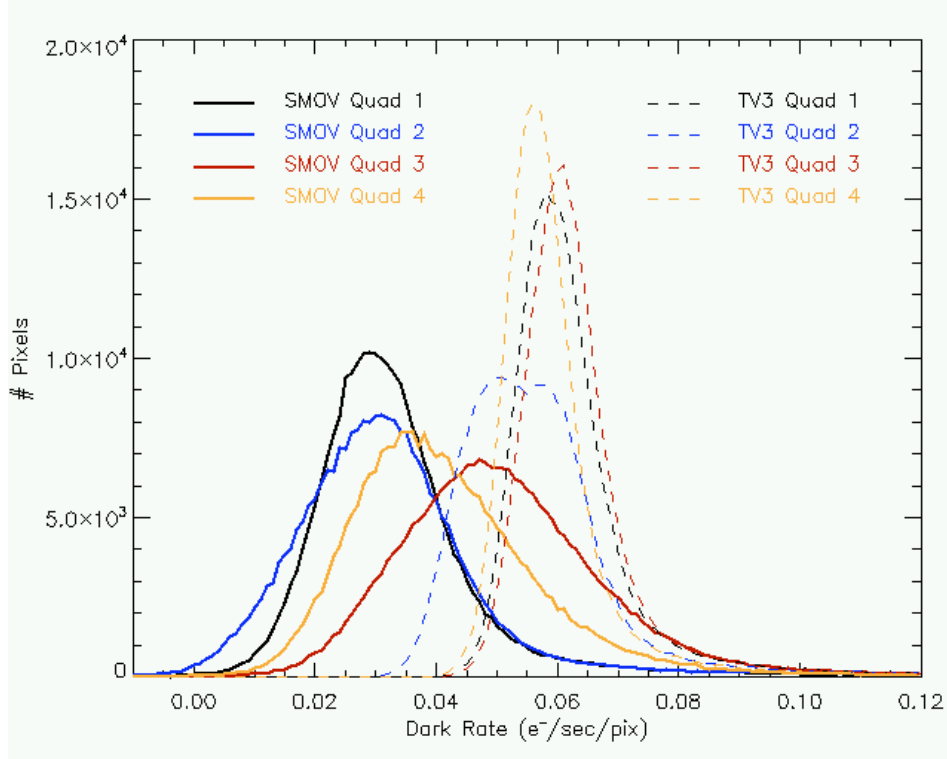


Figure 24: Dark current histogram for all four quadrants of the Visit 9 SPARS200 ramp (solid lines) as well as those from the mean SPARS200 ramp from TV3 testing (dashed lines). TV3 values have been converted to the gain values measured in SMOV, for ease of comparison. The dark current for the SMOV ramp is significantly lower than that from TV3.

<b>MEB2 Median Dark Current and Uncertainty (e<sup>-</sup>/sec/pixel)</b>				
	Quadrant 1	Quadrant 2	Quadrant 3	Quadrant 4
SPARS200 SMOV	0.030 / 0.011	0.030 / 0.013	0.048 / 0.016	0.037 / 0.015
SPARS200 TV3	0.059 / 0.007	0.053 / 0.010	0.060 / 0.007	0.056 / 0.006

Table 5: Mean IR dark current values for SPARS200 ramps. SMOV values are from the Visit 9 ramp. TV3 values are from the mean ramps derived from all TV3 data, and adjusted to use SMOV gain values for ease of comparison.

In an attempt to further investigate the lower than expected dark current in the IR channel, we attempted to extract reads unaffected by light leak from the other SPARS200 ramps taken in this proposal. This was done by examining HST orientation and pointing plots, such as that shown in Figure 6, for all SPARS200 darks in this proposal.

Using these plots, we were able to tentatively identify portions of ramps that were not affected by light leaks from the bright Earth. We then attempted to use the same method described above to calculate the dark rate in these partial ramps, and compare the results to the Visit 9 data. Figure 25 shows the measured dark rates for the SPARS200 ramps.

From this, we see that the Visit 9 appears to have an anomalously low dark current compared to other SMOV data. As the dark current rates for the other Visits were derived from partial ramps that may have been subjected to light leaks effects, we do not quote these as representative of the IR channel. Instead, we wait for results from proposal 11447 to discuss details of the IR channel dark rate. From these data, we note that the dark current in the IR channel appears to be roughly consistent with ground testing results.

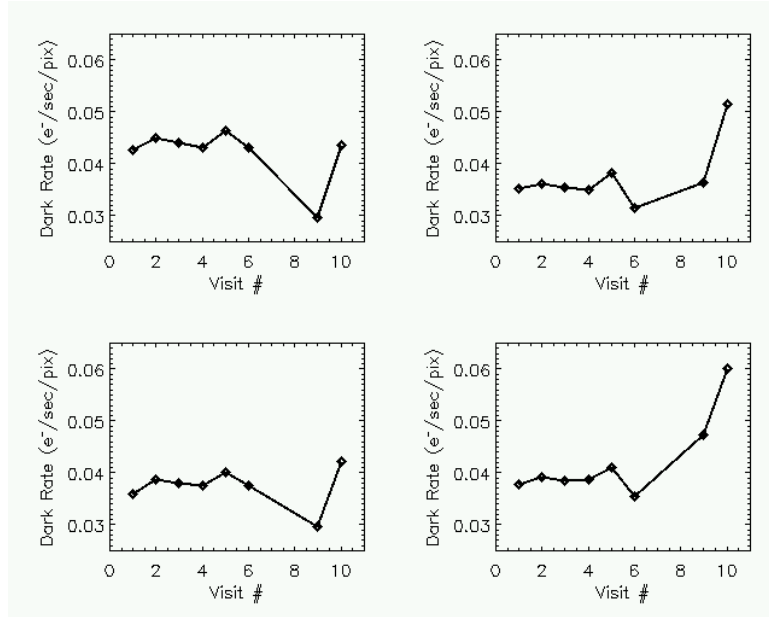


Figure 25: Measured dark current rates from partial ramps of SPARS200 data. Visit 9 does appear to be anomalously low, although other ramps may still be suffering from light leak effects.

We also investigated statistics on anomalous pixels in the IR detector. SPARS200 ramps are useful for this task as they use the longest SPARS sample sequence, which gives good signal to noise for the dark current and hence yields the most accurate count of anomalous pixels. Table 6 shows that the SMOV statistics are similar to those derived from a mean TV3 ramp. Not only are the statistics of anomalous pixels similar in SMOV as TV3, the vast majority of the anomalous pixels are indeed the very same pixels in the two circumstances. That is, the detector is exhibiting similar behavior now in orbit as it did on the ground; it appears that launching the instrument has not created a large number of “new” bad pixels (308), nor miraculously fixed any large number of “old” bad pixels (3452). Given the anomalously low mean dark current in the Visit 9 SMOV ramp, we will repeat this analysis on the dark ramps collected in proposal 11447 in order to obtain more reliable statistics.

<b>Percentage of Non-nominal Pixels MEB2: SMOV/TV3</b>				
	<b>Above CEI</b>	<b>Hot Pixels</b>	<b>Dark Pixels</b>	<b>Negative Pixels</b>
<b>SPARS200</b>				
Quad 1	0.9 / 1.0	0.6 / 0.6	0.8 / 0.03	0.7 / 0.4
Quad 2	0.7 / 0.7	0.4 / 0.4	3.8 / 0.01	0.6 / 0.04
Quad 3	0.5 / 0.5	0.3 / 0.3	0.1 / 0.01	0.1 / 0.04
Quad 4	0.5 / 0.6	0.3 / 0.3	0.3 / 0.02	0.3 / 0.2

Table 6: Fraction of light-sensitive pixels with non-nominal behaviors. All from SPARS200 data; pairs of elements are presented as “SMOV value / TV3 value” each in percent. TV3 values are from the current SPARS200 reference file (t611932fi\_drk.fits). The first column represents pixels with dark current values greater than the CEI Spec value of 0.4 e<sup>-</sup>/sec/pixel. The hot pixel column is for those pixels with dark current greater than 1.0 e<sup>-</sup>/sec/pixel. Dark pixels are those with dark current less than 0.01 e<sup>-</sup>/sec/pixel and greater than zero, and negative pixels are those with dark current values less than 0 e<sup>-</sup>/sec/pixel.

## Conclusions

The IR Channel in WFC3 during SMOV performs essentially as it did during TV3. Average dark current and read noise measured in SMOV (available in the abstract and Tables 3 and 4) are similar to those measured in TV3. Light leaks limited the amount of data with which we could measure the dark current. A better measure will be made using the data from proposal 11447, as well as the Cycle 17 dark monitoring program (11929). The spatial distribution, i.e. the 2-D pattern, of dark current (Figure 1) and flat field (Figure 2) are both similar to that observed in TV3. The anomalous pixel population appears largely unchanged from TV3 to SMOV (Table 6). Again, a better study of the various populations of pixels will be made with 11447 data. The gain measured during SMOV (2.28 – 2.47 ± 0.03 e<sup>-</sup>/ADU) is significantly different on a quadrant-to-quadrant basis than that measured in TV3 (2.31 – 2.38 e<sup>-</sup>/ADU), due to an improvement in the calculation method.

## Unresolved Issues

The analysis performed on the data from this proposal produced several questions that have yet to be fully answered. We list these here, in an effort to highlight them as issues in need of further study.

First, we found that the median 64 x 64 pixel subarray flat field image had a lower signal rate than the same pixels in the median full frame flat field by 3%. The same is true of the other subarray sizes, although to a lesser extent. The source of this difference is still not known. Also, a ratio of on-orbit to ground testing internal full frame flat fields shows quadrant to quadrant offsets in the mean level. This implies a difference in sensitivity from quadrant to quadrant between TV3 and SMOV?

The dark current rates listed in this report are derived from the only SPARS200 ramp that was unaffected by light leak from the bright Earth. However, this ramp shows anomalously low dark current relative to the portions of the other ramps unaffected by the light leak, as well as the dark currents measured in TV3 testing. What could cause this decrease in dark current, which was constant for the 2800 seconds of the ramp?

As was observed in TV3 testing, we note that when the IR channel is used to collect a series of nominally identical flat field images, much of the time the mean signal in the first ramp of the set will be depressed relative to subsequent ramps. We observed this behavior in all of the full frame flat fields, but only some of the 512 x 512 and 256 x 256 subarrays. Could this be due to persistence, or perhaps a reset issue with the detector?

Finally, Figure 26 is an enlarged version of the lower signal area of Figure 5. For LOS angle  $> 0$ , the flux is greater when HST is flying over dark Earth (+ symbols) than when it is flying over bright Earth (solid circles); this effect should be examined with more carefully and with more data. Possible causes include scattering of the OH-brightness from below, a voltage change associated with battery power (at night) compared to solar arrays (day)?

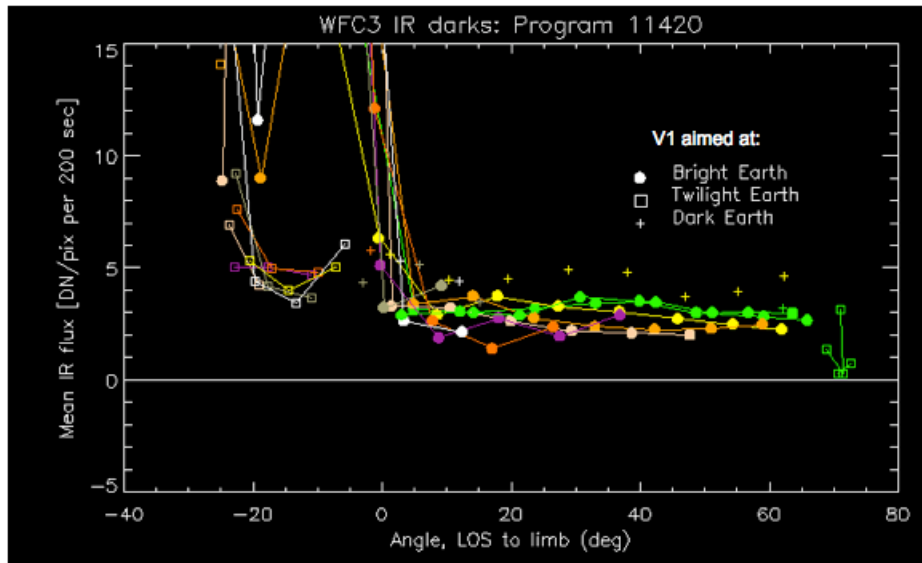


Figure 26: Same as previous figure, but with expanded vertical scale. The rise of the U-shaped trend of the twilight curves presumably is brighter twilight at left, by continuity with the bright Earth that preceded it in time, and then brightening at right (LOS angle  $\sim 5$  deg) due to the larger column density of atmosphere at grazing angles of incidence.

## References

- Baggett, S., 2009, *WFC3 SMOV Proposals 11423/11543: IR FSM and Lamp Checks*, WFC3 ISR 2009-28. <http://www.stsci.edu/hst/wfc3/documents/ISRs/WFC3-2009-28.pdf> Nov 2009.
- Bond, H. E., and Kim Quijano, J., et al. 2007, "Wide Field Camera 3 Instrument Handbook, Version 1.0" (Baltimore: STScI)
- Brown, T., 2008, *WFC3 TV3 Testing: IR Channel Throughput*. WFC3 ISR 2008-09. <http://www.stsci.edu/hst/wfc3/documents/ISRs/WFC3-2008-09.pdf> May 2008.
- Hilbert, B., 2008a, *WFC3 TV3 Testing: IR Channel Read Noise*. WFC3 ISR 2008-25. <http://www.stsci.edu/hst/wfc3/documents/ISRs/WFC3-2008-25.pdf> July 2008.
- Hilbert, B., 2008b, *WFC3 TV3 Testing: IR Channel Dark Current*. WFC3 ISR 2008-30. <http://www.stsci.edu/hst/wfc3/documents/ISRs/WFC3-2008-30.pdf> Sept 2008.
- Hilbert, B., 2008c, *WFC3 TV3 Testing: IR Gain Results* WFC3 ISR 2008-50. <http://www.stsci.edu/hst/wfc3/documents/ISRs/WFC3-2008-50.pdf> Dec 2008.
- Hilbert, B., 2008d, *WFC3 TV3 Testing: IR Channel Thermal Background Signal*. WFC3 ISR 2008-24. <http://www.stsci.edu/hst/wfc3/documents/ISRs/WFC3-2008-24.pdf> Dec 2008.
- Hilbert, B. and P. McCullough, 2009, *WFC3 SMOV Program 11447: IR Channel Dark Current, Readnoise, and Background Signal*. WFC3 ISR 2009-21. <http://www.stsci.edu/hst/wfc3/documents/ISRs/WFC3-2009-21.pdf> Nov 2009.
- McCullough, P., 2008, *Inter-pixel capacitance: prospects for deconvolution*. WFC3 ISR 2008-26. <http://www.stsci.edu/hst/wfc3/documents/ISRs/WFC3-2008-26.pdf> Aug 2008.
- McCullough, P., *Tools for predicting HST's orientation with respect to Earth*, in press.
- Robberto, M., 2008, *Thermal Vacuum 2: measures of the IR background and on-orbit predictions (SMS IR01S18)*. WFC3 ISR 2008-20. <http://www.stsci.edu/hst/wfc3/documents/ISRs/WFC3-2008-20.pdf> July 2008.

## Appendix 1

Table 7: Details of the data ramps collected for proposal 11420. The day and time columns refer to the day and time of the data collection. Files listed in bold and italics were contaminated by light leaks.

Day	Time	Visit	File	Filter	Target	Sample Sequence	Nsamp	Exposure Time (sec)	Array Size (pixels)
24-Jun	1:00	21	<i>iabg21a1q</i>	Blank	DARK	RAPID	5	0.30	64
24-Jun	1:00	21	<i>iabg21a2q</i>	Blank	DARK	RAPID	5	0.30	64
24-Jun	1:01	21	<i>iabg21a3q</i>	Blank	DARK	RAPID	5	0.30	64
24-Jun	1:01	21	<i>iabg21a4q</i>	Blank	DARK	RAPID	5	0.30	64
24-Jun	1:01	21	<i>iabg21a5q</i>	Blank	DARK	RAPID	5	0.30	64
24-Jun	1:02	21	<i>iabg21a6q</i>	Blank	DARK	RAPID	5	0.30	64
24-Jun	1:02	21	<i>iabg21a7q</i>	Blank	DARK	RAPID	5	0.30	64
24-Jun	1:02	21	<i>iabg21a8q</i>	Blank	DARK	RAPID	5	0.30	64
24-Jun	1:02	21	<i>iabg21a9q</i>	Blank	DARK	RAPID	5	0.30	64
24-Jun	1:03	21	<i>iabg21aaq</i>	Blank	DARK	RAPID	5	0.30	64
24-Jun	1:03	21	<i>iabg21abq</i>	Blank	DARK	RAPID	5	0.56	128
24-Jun	1:03	21	<i>iabg21acq</i>	Blank	DARK	RAPID	5	0.56	128
24-Jun	1:04	21	<i>iabg21adq</i>	Blank	DARK	RAPID	5	0.56	128
24-Jun	1:04	21	<i>iabg21aeq</i>	Blank	DARK	RAPID	5	0.56	128
24-Jun	1:04	21	<i>iabg21afq</i>	Blank	DARK	RAPID	5	0.56	128
24-Jun	1:05	21	<i>iabg21agq</i>	Blank	DARK	RAPID	5	0.56	128
24-Jun	1:06	21	<i>iabg21aiq</i>	Blank	DARK	RAPID	5	0.56	128
24-Jun	1:06	21	<i>iabg21ajq</i>	Blank	DARK	RAPID	5	0.56	128
24-Jun	1:07	21	<i>iabg21akq</i>	Blank	DARK	RAPID	5	0.56	128
24-Jun	1:07	21	<i>iabg21alq</i>	Blank	DARK	RAPID	5	0.56	128
24-Jun	1:07	21	<i>iabg21amq</i>	Blank	DARK	RAPID	5	1.39	256
24-Jun	1:07	21	<i>iabg21anq</i>	Blank	DARK	RAPID	5	1.39	256
24-Jun	1:08	21	<i>iabg21aoq</i>	Blank	DARK	RAPID	5	1.39	256
24-Jun	1:08	21	<i>iabg21apq</i>	Blank	DARK	RAPID	5	1.39	256
24-Jun	1:08	21	<i>iabg21aqq</i>	Blank	DARK	RAPID	5	1.39	256
24-Jun	1:09	21	<i>iabg21arq</i>	Blank	DARK	RAPID	5	1.39	256
24-Jun	1:09	21	<i>iabg21asq</i>	Blank	DARK	RAPID	5	1.39	256
24-Jun	1:09	21	<i>iabg21atq</i>	Blank	DARK	RAPID	5	1.39	256
24-Jun	1:10	21	<i>iabg21auq</i>	Blank	DARK	RAPID	5	1.39	256
24-Jun	1:10	21	<i>iabg21avq</i>	Blank	DARK	RAPID	5	1.39	256
24-Jun	1:11	21	<i>iabg21awq</i>	Blank	DARK	RAPID	5	4.27	512
24-Jun	1:11	21	<i>iabg21axq</i>	Blank	DARK	RAPID	5	4.27	512
24-Jun	1:14	21	<i>iabg21azq</i>	Blank	DARK	RAPID	5	4.27	512
24-Jun	1:15	21	<i>iabg21b0q</i>	Blank	DARK	RAPID	5	4.27	512
24-Jun	1:15	21	<i>iabg21b1q</i>	Blank	DARK	RAPID	5	4.27	512

24-Jun	1:16	21	iabg21b2q	Blank	DARK	RAPID	5	4.27	512
24-Jun	1:16	21	iabg21b3q	Blank	DARK	RAPID	5	4.27	512
24-Jun	1:16	21	iabg21b4q	Blank	DARK	RAPID	5	4.27	512
24-Jun	1:17	21	iabg21b5q	Blank	DARK	RAPID	5	4.27	512
24-Jun	1:17	21	iabg21b6q	Blank	DARK	RAPID	5	4.27	512
24-Jun	1:53	1	iabg01bfq	Blank	DARK	RAPID	15	43.98	1024
24-Jun	1:54	1	<b>iabg01bgq</b>	Blank	DARK	SPARS200	15	2802.94	1024
24-Jun	3:35	2	iabg02bqq	Blank	DARK	RAPID	15	43.98	1024
24-Jun	3:36	2	<b>iabg02brq</b>	Blank	DARK	SPARS200	15	2802.94	1024
24-Jun	5:15	3	iabg03c1q	Blank	DARK	RAPID	15	43.98	1024
24-Jun	5:16	3	<b>iabg03c2q</b>	Blank	DARK	SPARS200	15	2802.94	1024
24-Jun	6:55	4	iabg04ccq	Blank	DARK	RAPID	15	43.98	1024
24-Jun	6:57	4	<b>iabg04cdq</b>	Blank	DARK	SPARS200	15	2802.94	1024
24-Jun	8:35	5	iabg05diq	Blank	DARK	RAPID	15	43.98	1024
24-Jun	8:36	5	<b>iabg05djg</b>	Blank	DARK	SPARS200	15	2802.94	1024
24-Jun	10:15	6	iabg06dsq	Blank	DARK	RAPID	15	43.98	1024
24-Jun	10:16	6	<b>iabg06dtg</b>	Blank	DARK	SPARS200	15	2802.94	1024
24-Jun	12:50	31	iabg31e2q	F125W	TUNGSTEN	RAPID	15	43.98	1024
24-Jun	12:51	31	iabg31e3q	F125W	TUNGSTEN	RAPID	15	43.98	1024
24-Jun	13:03	31	iabg31e5q	F125W	TUNGSTEN	RAPID	15	43.98	1024
24-Jun	13:04	31	iabg31e6q	F125W	TUNGSTEN	RAPID	15	43.98	1024
24-Jun	13:16	31	iabg31e8q	F125W	TUNGSTEN	RAPID	15	43.98	1024
24-Jun	13:17	31	iabg31e9q	F125W	TUNGSTEN	RAPID	15	43.98	1024
24-Jun	13:29	31	iabg31ebq	F125W	TUNGSTEN	RAPID	15	43.98	1024
24-Jun	13:30	31	iabg31ecq	F125W	TUNGSTEN	RAPID	15	43.98	1024
24-Jun	13:42	31	iabg31eeq	F125W	TUNGSTEN	RAPID	15	43.98	1024
24-Jun	13:43	31	iabg31efq	F125W	TUNGSTEN	RAPID	15	43.98	1024
24-Jun	13:44	31	<b>iabg31egq</b>	F125W	TUNGSTEN	RAPID	15	0.91	64
24-Jun	13:44	31	<b>iabg31ehq</b>	F125W	TUNGSTEN	RAPID	15	0.91	64
24-Jun	13:45	31	<b>iabg31eiq</b>	F125W	TUNGSTEN	RAPID	15	0.91	64
24-Jun	13:45	31	<b>iabg31ejq</b>	F125W	TUNGSTEN	RAPID	15	0.91	64
24-Jun	13:56	31	<b>iabg31elq</b>	F125W	TUNGSTEN	RAPID	15	0.91	64
24-Jun	13:56	31	<b>iabg31emq</b>	F125W	TUNGSTEN	RAPID	15	0.91	64
24-Jun	13:57	31	<b>iabg31enq</b>	F125W	TUNGSTEN	RAPID	15	0.91	64
24-Jun	13:57	31	<b>iabg31eoq</b>	F125W	TUNGSTEN	RAPID	15	0.91	64
24-Jun	13:57	31	<b>iabg31epq</b>	F125W	TUNGSTEN	RAPID	15	0.91	64
24-Jun	13:58	31	<b>iabg31eqq</b>	F125W	TUNGSTEN	RAPID	15	0.91	64
24-Jun	13:59	31	<b>iabg31esq</b>	F125W	TUNGSTEN	RAPID	15	1.69	128
24-Jun	13:59	31	<b>iabg31etq</b>	F125W	TUNGSTEN	RAPID	15	1.69	128
24-Jun	13:59	31	<b>iabg31euq</b>	F125W	TUNGSTEN	RAPID	15	1.69	128
24-Jun	14:00	31	<b>iabg31evq</b>	F125W	TUNGSTEN	RAPID	15	1.69	128
24-Jun	14:00	31	<b>iabg31ewq</b>	F125W	TUNGSTEN	RAPID	15	1.69	128
24-Jun	14:00	31	<b>iabg31exq</b>	F125W	TUNGSTEN	RAPID	15	1.69	128
24-Jun	14:02	31	<b>iabg31ezq</b>	F125W	TUNGSTEN	RAPID	15	1.69	128
24-Jun	14:02	31	<b>iabg31f0q</b>	F125W	TUNGSTEN	RAPID	15	1.69	128
24-Jun	14:03	31	<b>iabg31f1q</b>	F125W	TUNGSTEN	RAPID	15	1.69	128
24-Jun	14:03	31	<b>iabg31f2q</b>	F125W	TUNGSTEN	RAPID	15	1.69	128

24-Jun	14:03	31	iabg31f3q	F125W	TUNGSTEN	RAPID	15	4.17	256
24-Jun	14:04	31	iabg31f4q	F125W	TUNGSTEN	RAPID	15	4.17	256
24-Jun	14:06	31	iabg31f6q	F125W	TUNGSTEN	RAPID	15	4.17	256
24-Jun	14:06	31	iabg31f7q	F125W	TUNGSTEN	RAPID	15	4.17	256
24-Jun	14:07	31	iabg31f8q	F125W	TUNGSTEN	RAPID	15	4.17	256
24-Jun	14:07	31	iabg31f9q	F125W	TUNGSTEN	RAPID	15	4.17	256
24-Jun	14:07	31	iabg31faq	F125W	TUNGSTEN	RAPID	15	4.17	256
24-Jun	14:08	31	iabg31fbq	F125W	TUNGSTEN	RAPID	15	4.17	256
24-Jun	14:11	31	iabg31fdq	F125W	TUNGSTEN	RAPID	15	4.17	256
24-Jun	14:11	31	iabg31feq	F125W	TUNGSTEN	RAPID	15	4.17	256
24-Jun	14:12	31	iabg31ffq	F125W	TUNGSTEN	RAPID	15	12.80	512
24-Jun	14:12	31	iabg31fgq	F125W	TUNGSTEN	RAPID	15	12.80	512
24-Jun	14:13	31	iabg31fhq	F125W	TUNGSTEN	RAPID	15	12.80	512
24-Jun	14:13	31	iabg31fiq	F125W	TUNGSTEN	RAPID	15	12.80	512
24-Jun	14:20	31	iabg31fkq	F125W	TUNGSTEN	RAPID	15	12.80	512
24-Jun	14:21	31	iabg31flq	F125W	TUNGSTEN	RAPID	15	12.80	512
24-Jun	14:21	31	iabg31fmq	F125W	TUNGSTEN	RAPID	15	12.80	512
24-Jun	14:22	31	iabg31fnq	F125W	TUNGSTEN	RAPID	15	12.80	512
24-Jun	14:22	31	iabg31foq	F125W	TUNGSTEN	RAPID	15	12.80	512
24-Jun	14:23	31	iabg31fpq	F125W	TUNGSTEN	RAPID	15	12.80	512
24-Jun	14:32	31	iabg31frq	F126N	TUNGSTEN	SPARS50	10	452.94	1024
24-Jun	14:40	31	iabg31fsq	F126N	TUNGSTEN	SPARS50	10	452.94	1024
24-Jun	14:48	31	iabg31ftq	F126N	TUNGSTEN	SPARS50	10	452.94	1024
24-Jun	15:08	7	iabg07fvq	Blank	DARK	RAPID	15	43.98	1024
24-Jun	15:09	7	<b>iabg07fwq</b>	Blank	DARK	SPARS200	15	2802.94	1024
24-Jun	16:43	8	iabg08g5q	Blank	DARK	RAPID	15	43.98	1024
24-Jun	16:44	8	<b>iabg08g6q</b>	Blank	DARK	SPARS200	15	2802.94	1024
24-Jun	17:42	9	iabg09g9q	Blank	DARK	RAPID	15	43.98	1024
24-Jun	17:43	9	iabg09gaq	Blank	DARK	SPARS200	15	2802.94	1024
24-Jun	18:42	10	<b>iabg10gcq</b>	Blank	DARK	RAPID	15	43.98	1024
24-Jun	18:43	10	<b>iabg10gdq</b>	Blank	DARK	SPARS200	15	2802.94	1024

Tables 8 and 9 list the reference files used by CALWF3 to process the data collected in proposal number 11420.

<b>File</b>	<b>Filename</b>	<b>Purpose</b>
BPIXTAB	t291659ni_bpx.fits	Bad pixel table
CCDTAB	t2c16200i_ccd.fits	Detector calibration parameters
OSCNTAB	q911321mi_osc.fits	Detector overscan table
CRREJTAB	t3j1659ki_crr.fits	Cosmic ray rejection parameters
DARKFILE	*	Dark current correction ramp
NLINFIL	sbi18555i_lin.fits	Detector non-linearity corrections
GRAPHTAB	t2605492m_tmng.fits	HST graph table
COMPTAB	t6i1714pm_tmc.fits	HST components table

*Table 8: Reference files used for all ramps collected as part of proposal 11420. Darkfile names are listed in the table below, as we have a different dark current calibration file for each sample sequence and subarray size. Files listed in both of these tables can be downloaded from the HST archive.*

<b>Sample Sequence</b>	<b>Array Size (pixels)</b>	<b>Dark File for CALWF3</b>
RAPID	1024 x 1024	t6119322i_drk.fits
	512 x 512	t5s1754di_drk.fits
	256 x 256	t5s1754ci_drk.fits
	128 x 128	t5s1754bi_drk.fits
	64 x 64	t5s1754ei_drk.fits
SPARS50	1024 x 1024	t611932ji_drk.fits

*Table 9: Dark current correction ramps used by CALWF3 when processing the internal flat field ramps taken as part of proposal 11420.*

## Appendix 2

We had not anticipated that looking at the bright Earth would compromise WFC3 IR dark current measurements. However, we have since learned that when HST is pointed at the bright Earth and the opaque BLANK is in place and the Channel Select Mechanism (CSM) is configured to reflect light toward the IR channel and away from the UVIS channel, the count rate on WFC3 IR can be as large as  $\sim 1$  e/s/pix. Three possibilities have been hypothesized for the light “leak”: 1) light leaking into the IR enclosure via the vent tube, 2) light warming the BLANK and its thermal radiation illuminating the IR detector, and 3) light passing into the IR cold enclosure’s window and leaking around the filter wheel inside the IR cold enclosure, entering the detector housing through its window, and illuminating the detector. The latter hypothesis is the preferred one, based upon the following analysis. See the Appendix 2 for diagrams giving the details of this light leak hypothesis.

In a separate calculation, we estimated that sunlit clouds of the bright Earth would produce  $0.3 \times 10^9$  photons/s/pixel on WFC3 IR with the F110W filter in place.<sup>2</sup> Using 2 eV/photon, an increase of  $\sim 4$ x for white light compared to F110W,  $1 \times 10^6$  pixels in the IR sensor, and assuming that the BLANK (at a pupil) receives light from  $\sim 2$ x more solid angle than the IR sensor’s f/11 field of view through HST, we estimate a conservative upper limit on the power  $P_{in}$  incident upon the BLANK to be  $\sim 1$  milliWatt:

$$P_{in} = 0.3 \times 10^9 * 2 * 4 * 1 \times 10^6 * 2 = 5 \times 10^{15} \text{ eV/s} = 0.8 \times 10^{-3} \text{ Watts.}$$

Alternatively, we can begin with the bolometric solar irradiance at Earth ( $0.1400 \text{ W/cm}^2$ ), assume the clouds scatter the Sun’s light in all directions like an integrating sphere, assume their albedo is unity, and hence the same irradiance is incident upon the HST primary mirror, and divide by the magnification 100-fold ratio of the WFC3 IR pupil to the pupil of HST.

---

<sup>2</sup> We neglect infrared light from the 300 K Earth because calculations indicate it is negligible compared to the solar reflected near-IR light and because the “leak” is observed to be much less when the V1 axis of HST aims at twilight Earth and the dark Earth compared to its bright Earth value, whereas the thermal-IR brightness of the Earth is nearly the same day or night.



Figure 27: The IR filter wheel. The BLANK, used for making dark current observations, is at the top of the wheel.

In the first few visits of program 11420, the bright Earth exposure was  $\sim 1000$  seconds, so  $\sim 1$  Joule was deposited on the BLANK during the Bright Earth period each HST orbit. The BLANK is an aluminum disk coated with de Soto black (Hilbert 2008). It appears to be grey in the photo shown in Figure 27, so for an upper limit we assume 10% of the incident light is absorbed by the aluminum BLANK, warms it up, and radiates thermally from its back side into the enclosure, which for this estimate we will scale from other estimates and observations as described shortly. Using a heat capacity for aluminum of 850 J/kg-K (at 250 K), and assuming the BLANK is a disk 0.5 cm thick and 2.5 cm in diameter (volume = 2.5 cm<sup>3</sup>; mass = 6.6x10<sup>-3</sup> kg), we expect 0.1 Joule to warm the BLANK by no more than 0.02 Kelvin. We expect 0.02 Kelvin to be negligible, because Stiavelli (2002) estimates that warming the dewar window, the refractive corrector, and a filter from -30 C to +20 C increases the count rate in J+H bands by 6.5 e<sup>-</sup>/s/pix, although primarily that is because of their small solid angle in his calculation. In a related estimate, Roberto (2008-20-2) states that the temperature of both the cold enclosure and the filter elements is -45 C. The ratio of blackbody radiance at -44 C, -35 C, and -25 C to that at -45 C is 1.2, 5, and 20. Since the contribution of the thermal emission from the BLANK is  $\sim 0.01$  e<sup>-</sup>/s/pixel greater than for a low-emissivity filter, we attribute 0.01 e<sup>-</sup>/s/pixel to be the thermal contribution from the BLANK (at -45 C) to the detector “dark” current (see Hilbert 2008d, Figure 1; Roberto 2008, Table 1). Therefore, increasing the BLANK’s temperature 20 K would increase its thermal load to the detector to 0.2 e<sup>-</sup>/s/pixel, i.e. even 1x10<sup>4</sup> times the estimated heating of the BLANK still wouldn’t explain the  $\sim 1$  e<sup>-</sup>/s/pixel “leak” observed when pointing at the bright Earth.

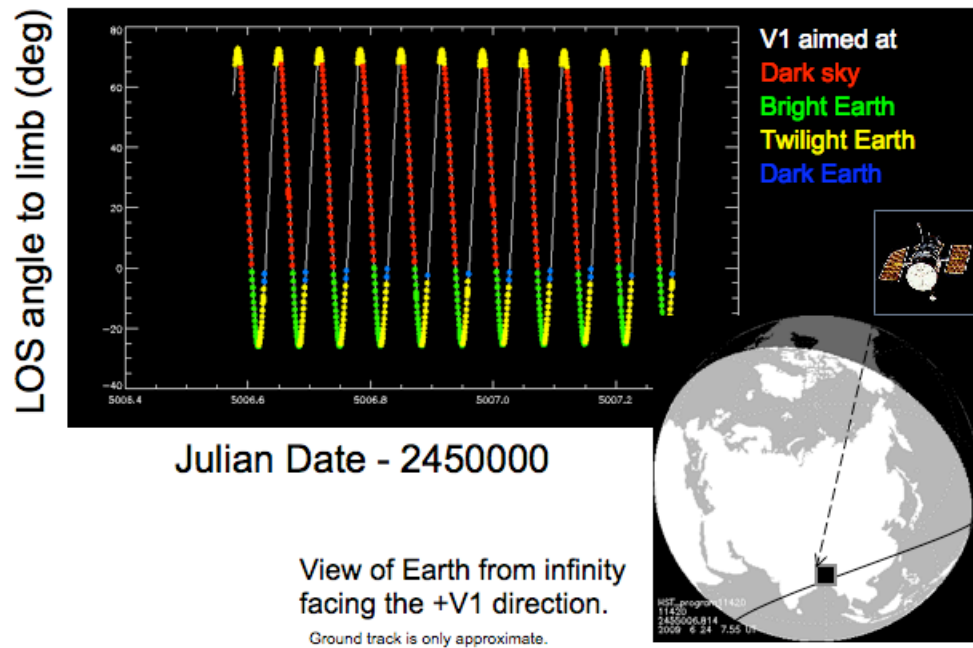


Figure 28: Geometry of Program 11420 of the initial execution on June 24, 2009 of the SPARS200 darks that exhibited the light leak described in the text. The view of Earth (inset) is from infinity facing the +V1 direction, i.e. facing the same direction as HST. The ground track is approximate and only illustrative of a typical HST pass.

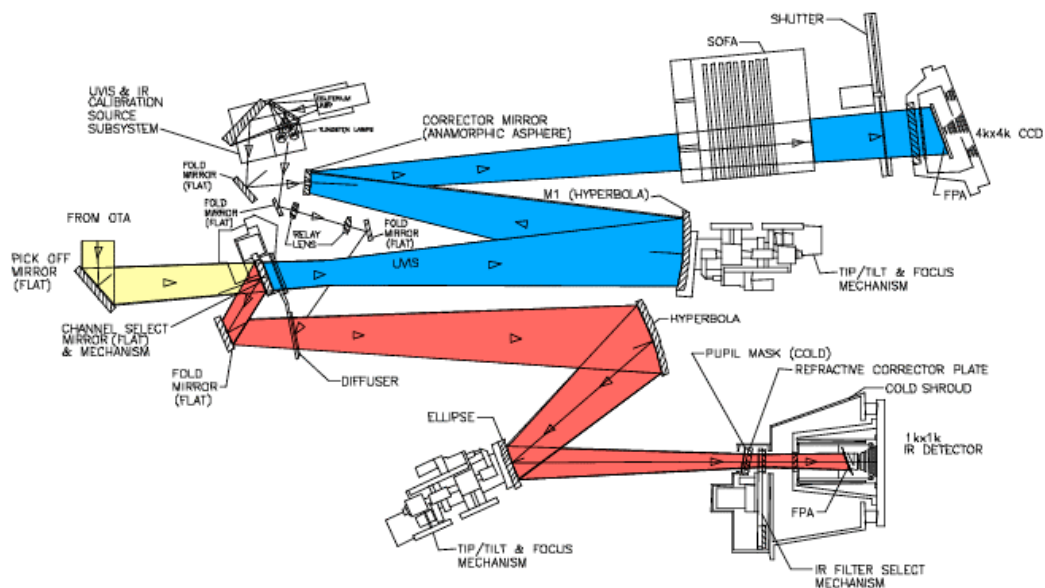


Figure 29: Schematic optical layout of WFC3 from its Instrument Handbook. The IR light leak path hypothesis involves light incident upon IR refractive corrector plate (labeled) scattering off and around the IR filter select mechanism (labeled) and ending its path at the IR focal plane assembly (labeled FPA).